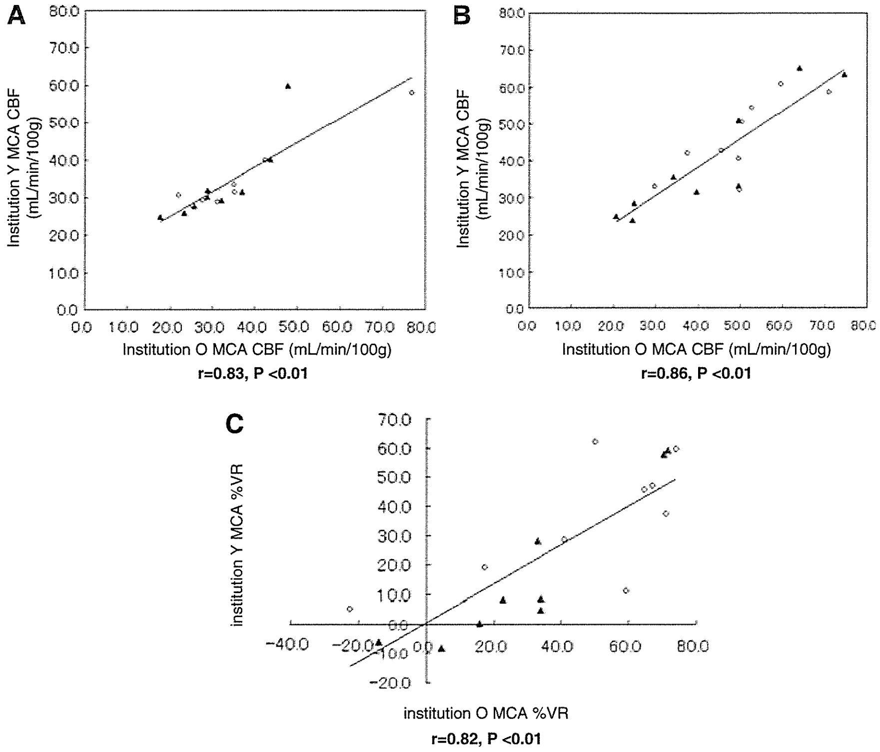

Figure 3 Scatter diagrams and regression lines of middle cerebral artery (MCA) cerebral blood flow (CBF) quantitation and percentage vascular reserve (%VR) in the two facilities. CBF quantitation and %VR in institutions O and Y are plotted on the *x*-axis and *y*-axis, respectively. Data are shown for the affected hemisphere (closed triangles) and the unaffected hemisphere (open circles). There were significant correlations between the two facilities for (**A**) CBF at rest (9 patients, $n = 18$ data points, $r = 0.83$, $P < 0.01$) (**B**) CBF after acetazolamide challenge (9 patients, $n = 18$, $r = 0.86$, $P < 0.01$), and (**C**) %VR for the affected and unaffected hemispheres (9 patients, $n = 18$, $r = 0.82$, $P < 0.01$).

cerebral ischemia, since this may contribute to prevention of recurrent ischemic stroke. To make further progress in this direction, techniques with broad versatility and standardized quantitation are required for large-scale studies.

Positron emission tomography can be used to assess the circulatory and metabolic states in the brain, but only a few facilities have installed PET systems and use of ^{15}O is not common; thus, the versatility of PET is low. In contrast, SPECT is used in most facilities and has broad versatility, but differences in models of γ-cameras and collimators may cause large interinstitutional differences. The QSPECT/DTARG method was developed to resolve errors caused by differences in SPECT models, and we have used this method in our group since December 2004. Such an image reconstruction method with high accuracy and improved quantitation may be helpful for determination of the indication and judgment of the effects of treatment in ischemic cerebral diseases and other diseases. In a multicenter trial, Iida *et al* (2010) found good reproducibility of QSPECT/DTARG. Correction of errors between facilities is also theoretically possible using this method, but this has not been verified by comparison of data from different clinical sites.

In this study, we verified that CBF values measured in nine patients with a cerebral artery stenotic lesion showed reproducibility between facilities. That is, these data showed significant correlations between facilities (institutions Y and O) for CBF at rest ($r = 0.83$, $P < 0.01$), CBF after acetazolamide challenge ($r = 0.86$, $P < 0.01$), CBF at rest and after acetazolamide challenge ($r = 0.91$, $P < 0.01$), and %VR ($r = 0.82$, $P < 0.01$). Good interobserver reliability was obtained, based on respective ICCs of 0.847 (95% CI: 0.634 to 0.940), 0.860 (0.656 to 0.946), 0.872 (0.764 to 0.932), and 0.727 (0.276 to 0.899). A GCA-9300A/PI $\tilde{a}$-camera with three detectors was used in institution Y, whereas an E.CAM $\tilde{a}$-camera with two detectors was used in institution O, and the collimators also differed between the institutions. Despite these differences, strong correlations were found between data collected at the two facilities. This finding is important for performance of multicenter studies. It is also important that the test protocol is strictly defined, as shown in Figure 1, and that the timings of agent administration and blood collection are sufficiently standardized. However, a good correlation was observed in data between the two institutions, both of which followed the test protocol, but there was a tendency for CBF in the higher flow region to

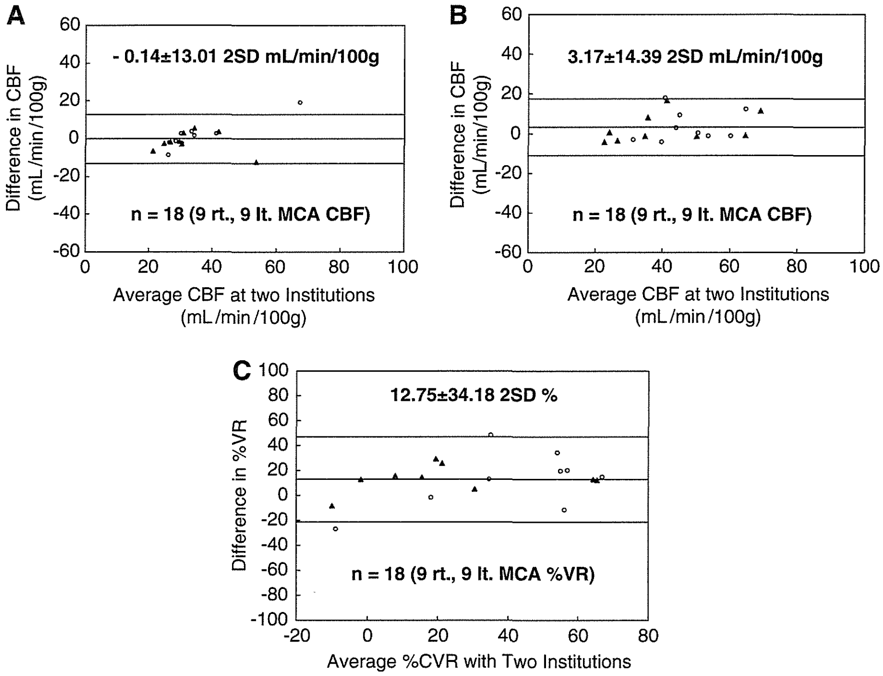

Figure 4 Bland–Altman plots of the consistency of middle cerebral artery (MCA) cerebral blood flow (CBF) measured in the two facilities. Data are shown for the affected hemisphere (closed triangles) and the unaffected hemisphere (open circles). Differences in CBF and percentage vascular reserve (%VR) were calculated as the value at institution O—that at institution Y. (**A**) CBF at rest (9 patients, $n = 18$ data points). A small bias was detected (mean difference, −0.14 mL per 100 g per minute) and the 2 s.d. was moderate (13.01 mL per 100 g per minute). (**B**) CBF after acetazolamide challenge (9 patients, $n = 18$). A small bias was detected (mean difference, 3.17 mL per 100 g per minute) and the 2 s.d. was moderate (14.39 mL per 100 g per minute). (**C**) %VR for the right and left hemispheres (9 patients, $n = 18$). A moderate bias was detected (mean difference, 12.75%) and the 2 s.d. was moderate (34.18%).

be lower at institution Y compared with institution O (Figures 3A and 3B). This might have happened because there was a minimum error when CBF of the same patient was determined with different γ-cameras and collimators using the QSPECT/DTARG method. A further limitation in the study may have been caused by the small sample size. In this study, we focused on data from MCA territories, but the results for the anterior cerebral artery and posterior cerebral artery also showed significant correlations (data not shown).

Good consistency of CBF was also obtained at the two facilities (Figure 4), but some measured values did fall outside the 2 s.d. range. These included one data point for CBF at rest (patient 7, Figure 4A), one after acetazolamide challenge (patient 8, Figure 4B), and two for %VR (patients 7 and 8, Figure 4C). In addition, as seen in Table 1, %VR for the right MCA in cases 7 and 8 at institution Y was significantly lower than that at institution O. In this study, there were no changes in the progress of symptoms and drug administration during the study period for all patients in the two facilities. Furthermore, there were no technical errors in performance of SPECT, time of drug administration, dosage, and leakage in injection. The differences in %VR for patients 7 and 8 suggest a progressive disease phase from the standpoint of cerebral circulation, despite no apparent clinical aggravation. As described above, there were two factors that might have caused the large 2 s.d. range in Figure 4C: the data for Cases 7 and 8 differed significantly between institutions O and Y (Table 1); and the results at institution Y seemed to be slightly lower than those at institution O (Figures 3A to 3C). It was difficult to eliminate intrinsic limitations such as aggravation of cerebral circulation and the reserve of the cerebral circulation because of the retrospective nature of the study. A prospective study with more subjects and a defined observation period is required to confirm the findings of this study.

The QSPECT/DTARG results suggest that this method can be used for objective evaluation as an indication for treatment of ischemic cerebral diseases. In addition, since the reproducibility is high, the method can be applied for observation of time-dependent changes in the same patient. In current medicine, ‘standardization’ has become important. Standardization of SPECT diagnosis of CBF is important to establish standard therapeutic policies for stroke prevention. This will be facilitated by improved accuracy of quantitative measurements using techniques such as QSPECT/DTARG and of diagnosis of severity using stereotaxic and quantitative image analysis such as SEE analysis. In the current study, CBF assessment with QSPECT/DTARG was significantly correlated between facilities and showed good reproducibility. This method may enable accurate determination of CBF and cerebrovascular reserve capacity at any institution, with standardization of the therapeutic index of patients with ischemic cerebral disease in terms of cerebral circulation.

Disclosure/conflict of interest

The authors declare no conflict of interest.

Acknowledgements

The authors are grateful for excellent technical assistance to Hideyuki Iwanaga and Yona Oishi.

References

Bland JM, Altman DG (1986) Statistical methods for assessing agreement between two methods of clinical measurement. *Lancet* 1:307–10

Frackowiak RS, Lenzi GL, Jones T, Heather JD (1980) Quantitative measurement of regional cerebral blood flow and oxygen metabolism in man using 15O and positron emission tomography: theory, procedure, and normal values. *J Comput Assist Tomogr* 4:727–36

Hatazawa J, Iida H, Shimosegawa E, Sato T, Murakami M, Miura Y (1997) Regional cerebral blood flow measurement with iodine-123-IMP autoradiography: normal values, reproducibility and sensitivity to hypoperfusion. *J Nucl Med* 38:1102–8

Hirano T, Minematsu K, Hasegawa Y, Tanaka Y, Hayashida K, Yamaguchi T (1994) Acetazolamide reactivity on 123I-IMP single photon emission computed tomography in patients with major cerebral artery occlusive disease: correlation with positron emission tomography parameters. *J Cereb Blood Flow Metab* 14:763–70

Iida H, Akutsu T, Endo K, Fukuda H, Inoue T, Ito H, Koga S, Komatani A, Kuwabara Y, Momose T, Nishizawa S, Odano I, Ohkubo M, Sasaki Y, Suzuki H, Tanada S, Toyama H, Yonekura Y, Yoshida T, Uemura K (1996) A multicenter validation of regional cerebral blood flow quantitation using [123I]iodoamphetamine and single photon emission computed tomography. *J Cereb Blood Flow Metab* 16:781–93

Iida H, Itoh H, Nakazawa M, Hatazawa J, Nishimura H, Onishi Y, Uemura K (1994) Quantitative mapping of regional cerebral blood flow using iodine-123-IMP and SPECT. *J Nucl Med* 35:2019–30

Iida H, Nakagawara J, Hayashida K, Fukushima K, Watabe H, Koshino K, Zeniya T, Eberl S (2010) Multicenter evaluation of a standardized protocol for rest and acetazolamide CBF assessment using quantitative SPECT reconstruction program and split-dose 123I-IMP. *J Nucl Med* 51:1624–31

Iida H, Narita Y, Kado H, Kashikura A, Sugawara S, Shoji Y, Kinoshita T, Ogawa T, Eberl S (1998) Effects of scatter and attenuation correction on quantitative assessment of regional cerebral blood flow with SPECT. *J Nucl Med* 39:181–9

Kai Y, Watanabe M, Morioka M, Hirano T, Yano S, Ohmori Y, Kawano T, Hamada J, Kuratsu J (2011) Cilostazol improves symptomatic intracranial artery stenosis – evaluation of cerebral blood flow with single photon emission computed tomography. *Surg Neurol Int* 2:8

Kim KM, Watabe H, Hayashi T, Hayashida K, Katafuchi T, Enomoto N, Ogura T, Shidahara M, Takikawa S, Eberl S, Nakazawa M, Iida H (2006) Quantitative mapping of basal and vasoreactive cerebral blood flow using split-dose 123I-iodoamphetamine and single photon emission computed tomography. *Neuroimage* 33:1126–35

Matsumoto S, Shimodozono M, Miyata R, Kawahira K (2011) Effect of cilostazol administration on cerebral hemodynamics and rehabilitation outcomes in post-stroke patients. *Int J Neurosci* 121:271–8

Minoshima S, Koeppe RA, Frey KA, Kuhl DE (1994) Anatomic standardization: linear scaling and nonlinear warping of functional brain images. *J Nucl Med* 35:1528–37

Mizumura S, Nakagawara J, Takahashi M, Kumita S, Cho K, Nakajo H, Toba M, Kumazaki T (2004) Three-dimensional display in staging hemodynamic brain ischemia for JET study: objective evaluation using SEE analysis and 3D-SSP display. *Ann Nucl Med* 18:13–21

Nakagawara J (1999) Clinical neuroimaging of cerebral ischemia. *No To Shinkei* 51:502–13

Nakagawara J, Hyogo T, Kataoka T, Hayase K, Kasuya J, Kamiyama K (2000) Role of neuroimaging (SPECT/PET, CT/MRI) in thrombolytic therapy. *No To Shinkei* 52:873–82

North American Symptomatic Carotid Endarterectomy Trial Collaborators (1991) Beneficial effect of carotid endarterectomy in symptomatic patients with high-grade carotid stenosis. *N Engl J Med* 325:445–53

Sato T, Hanyu H, Hirao K, Kanetaka H, Sakurai H, Iwamoto T (2011) Efficacy of PPAR-γ agonist pioglitazone in mild Alzheimer disease. *Neurobiol Aging* 32:1626–33

Yamauchi H, Fukuyama H, Nagahama Y, Nabatame H, Ueno M, Nishizawa S, Konishi J, Shio H (1999) Significance of increased oxygen extraction fraction in five-year prognosis of major cerebral arterial occlusive disease. *J Nucl Med* 40:1992–8

Yamauchi H, Kudoh T, Kishibe Y, Iwasaki J, Kagawa S (2007) Selective neuronal damage and chronic hemodynamic cerebral ischemia. *Ann Neurol* 61:454–65

Quantitative Evaluation of Cerebral Blood Flow and Oxygen Metabolism in Normal Anesthetized Rats: ^{15}O-Labeled Gas Inhalation PET with MRI Fusion

Tadashi Watabe[1,2], Eku Shimosegawa[1], Hiroshi Watabe[3], Yasukazu Kanai[3], Kohei Hanaoka[1], Takashi Ueguchi[4], Kayako Isohashi[1], Hiroki Kato[1], Mitsuaki Tatsumi[4], and Jun Hatazawa[1,2]

[1]Department of Nuclear Medicine and Tracer Kinetics, Osaka University Graduate School of Medicine, Suita, Osaka, Japan; [2]Immunology Frontier Research Center, Osaka University, Suita, Osaka, Japan; [3]Department of Molecular Imaging in Medicine, Osaka University Graduate School of Medicine, Suita, Osaka, Japan; and [4]Department of Radiology, Osaka University Hospital, Suita, Osaka, Japan

PET with ^{15}O gas has been used for the quantitative measurement of cerebral blood flow (CBF), cerebral metabolic rate of oxygen ($CMRO_2$), oxygen extraction fraction (OEF), and cerebral blood volume (CBV) in humans. However, several technical difficulties limit its use in experiments on small animals. Herein, we describe the application of the ^{15}O gas steady-state inhalation method for normal anesthetized rats. **Methods:** Eight normal male Sprague–Dawley rats (mean body weight ± SD, 268 ± 14 g) under anesthesia were investigated by ^{15}O-labeled gas PET. After tracheotomy, an airway tube was placed in the trachea, and the animals were connected to a ventilator (tidal volume, 3 cm^3; frequency, 60/min). The CBF and OEF were measured according to the original steady-state inhalation technique under artificial ventilation with ^{15}O-CO_2 and ^{15}O-O_2 gases delivered through the radioactive gas stabilizer. CBV was measured by ^{15}O-CO gas inhalation and corrected for the intravascular hemoglobin-bound ^{15}O-O_2. Arterial blood sampling was performed during each study to measure the radioactivity of the whole blood and plasma. MR image was performed with the same acrylic animal holder immediately after the PET. Regions of interest were placed on the whole brain of the PET images with reference to the semiautomatically coregistered PET/MR fused images. **Results:** The data acquisition time for the whole PET experiment in each rat was 73.3 ± 5.8 (range, 68–85) min. In both the ^{15}O-CO_2 and the ^{15}O-O_2 studies, the radioactivity count of the brain reached a steady state by approximately 10 min after the start of continuous inhalation of the gas. The quantitative PET data of the whole brain were as follows: CBF, 32.3 ± 4.5 mL/100 mL/min; $CMRO_2$, 3.23 ± 0.42 mL/100 mL/min; OEF, 64.6% ± 9.1%; and CBV, 5.05 ± 0.45 mL/100 mL. **Conclusion:** Although further technical improvements may be needed, this study demonstrated the feasibility of quantitative PET measurement of CBF, OEF, and $CMRO_2$ using the original steady-state inhalation method of ^{15}O-CO_2 and ^{15}O-O_2 gases and measurement of CBV using the ^{15}O-CO gas inhalation method in the brain of normal anesthetized rats.

Key Words: ^{15}O-gas PET; CBF; OEF; $CMRO_2$

J Nucl Med 2013; 54:283–290
DOI: 10.2967/jnumed.112.109751

Cerebral blood flow (CBF) and metabolic rate of oxygen ($CMRO_2$) have been extensively studied in humans using PET with ^{15}O-labeled gases and $H_2{}^{15}O$ to elucidate the brain functions (*1*) and hemodynamic and metabolic compromise in stroke patients (*2*). However, several difficulties restrict the application of this method to experimental animals.

The major difficulty of ^{15}O gas PET in small animals is related to the delivery of ^{15}O gas to the brain. Inhaled radioactive gases exist in the nasal and oral cavities and the lung, which may disturb accurate measurement of the intracranial radioactivity because of increased random coincidence events and scattered photons. The second is the limited volume of blood that can be sampled from small animals to measure the arterial input function, which is essential for quantitative analysis. The third is the limited volume of the tracer solution that can be injected into small animals. To overcome these technical difficulties, some previous studies have applied ^{15}O gas inhalation through a tracheal tube (*3*), venous injection of ^{15}O-O_2 hemoglobin–containing red blood cells (*4,5*), ^{15}O-CO or O_2 hemoglobin–containing vesicles (*6*), or liposome-encapsulated hemoglobin (*7*). For quantitative measurements, the radioactivity of the cardiac chambers has been measured (*3*). A β-probe was developed to directly measure the arterial input function, without any need for blood sampling (*8*). Furthermore, programmed injection devices have been developed to achieve steady-state radioactivity of the brain (*9*). However, there have been no reports of quantitative measurement of CBF, cerebral blood volume (CBV), oxygen extraction fraction (OEF), and $CMRO_2$ in the rat brain by ^{15}O-gas inhalation PET. The purpose of this study was to establish a standard methodology to evaluate the cerebral circulation and oxygen metabolism in rats, to allow the evaluation

---

Received Jun. 16, 2012; revision accepted Aug. 23, 2012.

For correspondence or reprints contact: Jun Hatazawa, 2-2 Yamadaoka, Suita, Osaka 565-0871 Japan.

E-mail: hatazawa@tracer.med.osaka-u.ac.jp

Published online Jan. 3, 2013

COPYRIGHT © 2013 by the Society of Nuclear Medicine and Molecular Imaging, Inc.

of cerebral ischemia in a rat model. We developed a method to measure CBF, CBV, OEF, and $CMRO_2$ in anesthetized rats according to the original ^{15}O gas steady-state inhalation method, which was used in clinical studies (*10–12*). We paid special attention to administration of the ^{15}O gases through the trachea under a steady-state supply of $^{15}O\text{-}CO_2$ and $^{15}O\text{-}O_2$. We describe here the feasibility of the method and the quantitative measurement of CBF, CBV, OEF, and $CMRO_2$ in the brains of normal rats under anesthesia. We performed all studies using a clinical PET camera. The feasibility of the PET camera for small-animal imaging was evaluated by phantom experiments as well.

MATERIALS AND METHODS

Preparation of ^{15}O Gas

^{15}O gas was produced by a $^{14}N(d,n)^{15}O$ nuclear reaction with 2.0% O_2 (for $^{15}O\text{-}CO$ and $^{15}O\text{-}O_2$) or 2.0% CO_2 (for $^{15}O\text{-}CO_2$) added to an N_2 gas target at a 12-MeV-proton 20-μA current accelerated by the CYPRIS HM 12S in-house cyclotron (Sumitomo Heavy Industry). The concentrations and flow rates of $^{15}O\text{-}O_2$, $^{15}O\text{-}CO$, and $^{15}O\text{-}CO_2$ were controlled by the CYPRIS gas stabilization module, G3-A (Sumitomo Heavy Industry). Flow volume from the gas stabilizer system was regulated by a mass flow controller to achieve a constant supply of radioactivity.

PET and MR Scanner

The PET study was performed with the Headtome-V PET scanner (Shimadzu Corp.). The performance of the scanner has been described previously (*13*). PET data were collected in 2-dimensional (2-D) mode (septa extended) and reconstructed by the 2-D filtered backprojection method with Butterworth filter (1-mm cutoff frequency). The spatial resolution was 4.0 mm in full width at half maximum (FWHM) in the transaxial direction and 4.5 mm in FWHM in the axial direction. The voxel size was 0.5 × 0.5 × 3.125 mm. The PET data were not corrected for attenuation or scatter.

The PET and MR studies were performed with an MR-compatible acrylic holder held at the same position in all the experiments. MR imaging was performed with the same holder immediately after the PET acquisition, using a permanent magnet MR imaging system of 0.3 T (Hitachi Metal; NEOMAX, Ltd.) (*14*). The MR imaging sequence was a fast low-angle shot (repetition time/echo time, 50/5 ms; 64 slices; field of view, 60 mm). Position shift between the PET and MR images was confirmed by a phantom experiment, and coregistration of the PET and MR images was automatically performed using in-house fusion software (gPET/MRI).

Estimation of Partial-Volume Effect

The body phantom of the National Electrical Manufacturers Association was used for the evaluation of the partial-volume effect. Five spheres of different sizes were placed inside the water (diameter, 10, 13, 17, 22, and 28 mm) and filled with $^{15}O\text{-}H_2O$ of the same radioactivity concentration. The scanning time was 15 min, and the PET images were reconstructed using a 2-D filtered backprojection method with attenuation correction. Regions of interest (ROIs) were placed on each sphere, and the mean count ratios to the 28-mm-diameter sphere were plotted against the diameter.

Effect of Attenuation Correction

Transmission scanning with a $^{68}Ge\text{–}^{68}Ga$ rod source was performed in the brain of a sacrificed rat to prepare an accurate attenuation map (scan duration, 167 min). The $^{15}O\text{-}O_2$ gas PET images were reconstructed both with and without attenuation correction. Profile curves of the brain count were compared between the images with and without attenuation correction.

Effect of Scatter Correction

The lung phantom (rubber balloon) was placed in the pleural cavity of a sacrificed rat after the lung was removed. PET was performed for 16 min under $^{15}O\text{-}O_2$ ventilation (100 MBq/min, 180 mL/min). Then, scatter radiation from the lung was evaluated.

Cross Calibration Factor

Because of the limited volume of the blood samples, we tested the linearity of the cross calibration factor against the volume of plasma measured by a well counter. The radioactivity concentrations of 0.01, 0.025, 0.05, 0.10, and 0.20 mL of $H_2{}^{15}O$ solution were measured by the well counter. The radioactivity concentrations were corrected for physical decay and weight and plotted against the weight.

Animal Preparation and PET Measurements

Normal male Sprague–Dawley rats from Japan SLC Inc. were used for this investigation. Eight rats (8 wk old; mean body weight ± SD, 268 ± 14 g) were anesthetized with 2% isoflurane plus 100% oxygen during the arterial cannulation, followed later by intramuscular injection of midazolam (1.2 mg/kg of body weight), xylazine (4.8 mg/kg of body weight), and butorphanol (1.6 mg/kg of body weight). Arterial cannulation was performed on the femoral artery using a 0.8-mm polythene tube ($n = 6$) or on the tail artery using a Terumo 24-gauge indwelling catheter ($n = 2$). Tracheotomy was performed, and a flexible tube (6-French, 5 cm; Hanako Medical Products) was placed into the trachea to serve as an airway for the administration of ^{15}O-gas. The airway tube was connected to the ventilator (SN-480-7-10; Shinano Seisakusho), and artificial ventilation was performed with room air (tidal volume, 3 cm^3; frequency, 60/min). The rats were placed supine on the bed, and the airway tube was flexed to the distal side to exclude it from the transaxial field of view of the brain.

$^{15}O\text{-}CO_2$, $^{15}O\text{-}O_2$, and $^{15}O\text{-}CO$ gas were administered, where the order of $^{15}O\text{-}O_2$ and $^{15}O\text{-}CO_2$ studies was randomized, with room air as the carrier (50, 100, and 100 MBq/min, respectively). The flow volume and radioactivity concentration were automatically maintained through the stabilization module, which was directly connected to the artificial ventilator. The PET measurements were started with the administration of each ^{15}O-labeled gas. Inhalation of the $^{15}O\text{-}CO_2$ and $^{15}O\text{-}O_2$ gas was continued during the PET measurements for 16 min (60 s × 16 frames). The inhalation time of the $^{15}O\text{-}CO$ gas was 3 min, and the PET measurements were continued for a total of 12 min (60 s × 12 frames). Arterial blood sampling (0.1 mL) was performed from the arterial cannula during the steady-state PET acquisition in the $^{15}O\text{-}CO_2$ and $^{15}O\text{-}O_2$ studies (13 and 16 min after the start of scanning, respectively) and 7 min after the start of the scanning in the $^{15}O\text{-}CO$ study. The radioactivity and weight of the whole blood and plasma after centrifugation (3,000 round/min, 3 min) were measured with a well scintillation counter (BeWell; Molecular Imaging Labo), and the radioactivity concentration of each blood sample (cps [count per second]) was corrected for the decay from the sampling time.

Systemic blood pressure (BP) and heart rate (HR) were indirectly measured with a tail-cuff apparatus during the study (BP-98A-L; Softron). Arterial blood gas was analyzed using the blood samples collected during the $^{15}O\text{-}CO_2$ and $^{15}O\text{-}O_2$ PET acquisition (i-STAT system; Abbott Point of Care Inc.), and pH, partial pressures of carbon dioxide ($PaCO_2$) (mm Hg), partial pressures of oxygen (PaO_2) (mm Hg), arterial oxygen saturation (SaO_2) (%), hemoglobin (Hb) (g/dL), and hematocrit (Ht) (%) were measured. The rectal temperature was also monitored and automatically maintained at 37° with a body heating pad system (TR-200; Muromachi Kikai Co., Ltd.).

Experiments in Ischemia Model

In 2 rats, the left middle cerebral artery (MCA) was occluded intraluminally by inserting a nylon 4-0 surgical monofilament with dental impression material into the left common carotid artery (*15*). PET was performed at 30 min after the occlusion without reperfusion.

All animal experiments were performed in compliance with the guidelines of the Laboratory Investigation Committee of Osaka University Graduate School of Medicine.

Quantitative Data Calculation

Regional CBF, regional OEF, and regional $CMRO_2$ were calculated by the steady-state method (*11,12*). Regional CBV was calculated after brief administration by inhalation of ^{15}O-CO gas, which was tightly bound to hemoglobin. In the ^{15}O-CO_2 study, the activity measured in the brain was from ^{15}O-labeled water, which was transferred from $C^{15}O_2$ to $H_2{}^{15}O$ in the pulmonary alveolar capillaries. In the ^{15}O-O_2 study, the activity in the brain was considered to be a sum of 3 components: ^{15}O-labeled water produced as a metabolite of ^{15}O-O_2 in the brain tissues, recirculating ^{15}O-labeled water, and ^{15}O-O_2 fixed to hemoglobin in the vascular compartment. Quantitative values were calculated using the following equations:

$$\text{regional CBF} = \lambda/(C_a/C_t - 1/\rho),$$

$$\text{regional OEF} = \left(C_t'/C_t \times C_a/C_p' - C_a/C_p\right)\Big/\left(C_a'/C_p' - C_a/C_p\right),$$

$$\text{regional } CMRO_2 = \text{CBF} \times \text{OEF} \times [\text{Total blood oxygen content}],$$

$$\text{regional CBV} = C_t''/\left(C_a'' \times f\right),$$

where λ (/min) is the decay constant of ^{15}O. C_a (Bq/g) is the $H_2{}^{15}O$ concentration in the whole blood, C_p (Bq/g) is the $H_2{}^{15}O$ concentration in the blood plasma, and C_t (Bq/mL) is the average brain radioactivity concentration without decay correction in the ^{15}O-CO_2 study. ρ is a brain–blood partition coefficient for water, fixed at 0.91 mL/g (*16*). C_a' (Bq/g) is the $H_2{}^{15}O$ and ^{15}O-O_2 concentration in the whole blood, C_p' (Bq/g) is the $H_2{}^{15}O$ concentration in the blood plasma, and C_t' (Bq/mL) is the average brain radioactivity concentration without decay correction in the ^{15}O-O_2 study. Total blood oxygen content was calculated using the following equation: 1.39 × Hb (g/dL) × SaO_2 (%)/100 + 0.0031 × PaO_2 (mm Hg). C_a'' (Bq/g) is the ^{15}O-CO concentration in the whole blood, and C_t'' (Bq/mL) is the average brain radioactivity concentration with decay correction in the ^{15}O-CO study. f is the correction value of the hematocrit between the great vessels and the brain, fixed at 0.70 (*17*). The CBV data were used to correct for intravascular hemoglobin-bound $^{15}O_2$ (*12*). Functional images of the CBF, $CMRO_2$, OEF, and CBV were reconstructed using the Shimadzu PET console system. ROIs ($0.86-1.08$ cm^2) were manually drawn on the whole brain of the 3 sequential cross-sectional CBF PET images, with reference to the semiautomatically coregistered PET/MR fused images (Fig. 1). The same ROIs were placed on other functional images as well. In the rat models of left MCA occlusion, oval ROIs were placed on the bilateral MCA territories and compared between the ipsilateral and contralateral sides.

RESULTS

Figure 2A shows the PET images of a spheric phantom filled with $H_2{}^{15}O$ water for the evaluation of partial-volume effect. The count ratios were 0.36, 0.54, 0.73, and 0.89 for spheres measuring 10, 13, 17, and 22 mm in diameter, respectively, as compared with the count for 28-mm spheres, which provided full recovery (Fig. 2B). Because the brain volume of rats corresponds to that of 15-mm spheres, the partial-volume effect for the whole brain was calculated as 0.7. Figure 3A shows a coronal PET image of the rat brain after $^{15}O_2$ inhalation during the steady state. The profile curves of radioactivity at the line passing the basal ganglia are illustrated with and without attenuation correction in Figure 3B. The profile curves with and without attenuation correction were identical. Figure 4 shows the coronal images of a lung phantom placed in the pleural cavity of a sacrificed rat ventilated with $^{15}O_2$ gas. High radioactivity was found in the pleural cavities bilaterally. No radioactivity from the lung phantom was detected in the brain, indicating that the effect of scatter events from the lung was small. Figure 5 shows a plot of the radioactivity (cps/g) concentrations against the sample volumes of the $H_2{}^{15}O$ solution by well counter. The radioactivity was constant for volumes in the range of 0.025–0.20 mL.

The mean systolic and diastolic BPs, PaO_2, $PaCO_2$, hemoglobin concentration, hematocrit, and SaO_2 are summarized in Table 1. The BP remained stable during the PET measurements.

The total time taken for the entire PET scan in each rat was 73.3 ± 5.8 (68–85) min. In both the ^{15}O-CO_2 and ^{15}O-O_2 studies, the radioactivity count in the brain reached a steady state approximately 10 min after continuous ^{15}O gas inhalation (Fig. 6).

Quantitative PET data in the entire brain were as follows: CBF, 32.3 ± 4.5 mL/100 mL/min; $CMRO_2$, 3.23 ± 0.42 mL/100 mL/min; OEF, 64.6% ± 9.1%; and CBV, 5.05 ± 0.45 mL/100 mL. Functional images of the CBF, $CMRO_2$, OEF, and CBV are shown in Figure 7.

For the findings in the rat model of left MCA occlusion, both rats showed decreased CBF and $CMRO_2$ in the ipsilateral MCA territory, and one of the rats showed increased OEF in the ipsilateral MCA territory. Quantitative values in the ipsilateral and contralateral MCA territories were as follows: CBF, 18.6/30.8 mL/100 mL/min; OEF, 74.3%/65.4%; and $CMRO_2$, 1.79/2.64 mL/100 mL/min.

DISCUSSION

We have reported a method to measure the CBF, CBV, OEF, and $CMRO_2$ in the brain of anesthetized rats by PET, according to the original ^{15}O-CO_2 and ^{15}O-O_2 steady-state inhalation technique combined with ^{15}O-CO inhalation. The methodology in this study is the same as the steady-state method used in clinical PET examinations (*10–12*).

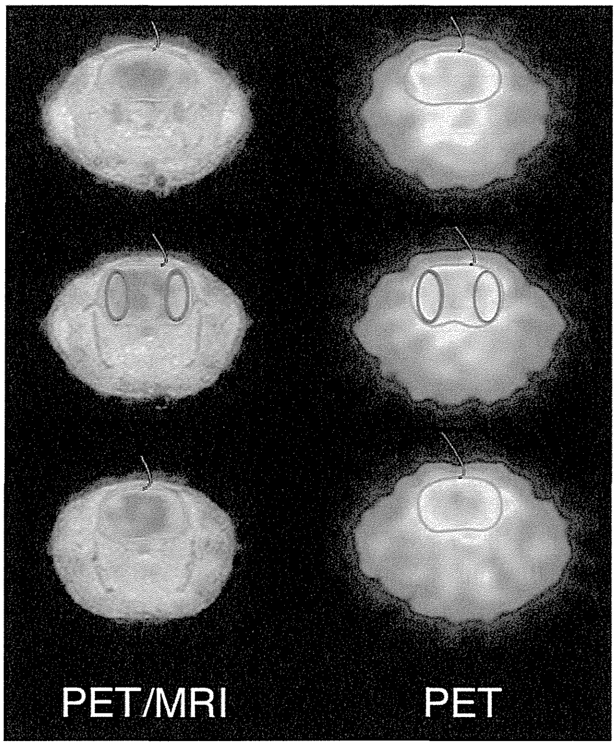

FIGURE 1. Location of ROIs on whole-brain PET slice at maximal cross-section and adjacent cranial and caudal slices. Green ROI = whole brain; red ROI = MCA territories.

Yee et al. performed tracheal administration of $^{15}O-O_2$ gas through a surgically placed airway tube in anesthetized rats (*3*). The $^{15}O-O_2$ was stored in a syringe (74–111 MBq, 5 cm^3) and insufflated into the lung. Their study indicated that $^{15}O-O_2$ administration through the trachea did not affect the image quality of the brain. Tracheotomy also had no significant influence on the physiologic conditions of the rats during the experiments. In our method, one end of the airway tube was inserted into the trachea after tracheotomy and fixed tightly to avoid leakage of the ^{15}O gases. The other end of the airway tube was connected to the ventilator, which continuously supplied the ^{15}O gases at a controlled rate of radioactivity. As shown in Figure 4, no radioactivity in the brain was detected during the ^{15}O-gas insufflation to the balloon phantoms located in the chest cavity. The present PET data acquisition in the 2-D mode was less sensitive to scatter events than acquisitions in the 3-dimensional mode. Quantitative measurement in 3-dimensional mode clinical PET can be achieved with proper scatter correction, just as in the 2-D mode (*18*). We intend to quantitatively measure ^{15}O gas in a 3-dimensional-mode small-animal PET study in the near future.

It is essential, in the ^{15}O gas steady-state inhalation method, to stabilize the radioactivity of the inhaled gases. Artificial ventilation was performed with a radioactive gas stabilization system in this study. The radioactivity distribution in the brain became stable by approximately 10 min after the start of the $^{15}O-CO_2$ and $^{15}O-O_2$ inhalation. There was a slight increase even after 10 min. The average increase of the count from 10 to 15 min was 3.4% in the CO_2 study and 3.7% in the O_2 study. These increases were relatively small as compared with the average variability in brain counts between 10 and 15 min (5.5%). We performed an experimental study for continuous monitoring of arterial BP in 3 rats. Systemic BP had been generally stable from 15 to 90 min after the start of anesthesia (data not shown). The biologic half-life of xylazine is 2–3 h in rats, which is sufficiently long to maintain a stable condition during the PET measurements.

In this study, 2 rats underwent $^{15}O-O_2$ scanning before $^{15}O-CO_2$ scanning, and the other rats were scanned in the opposite order. No systematic changes in CBF, OEF, or $CMRO_2$ dependent on the order of scanning were observed.

The whole-body blood volume of the rats weighing about 300 g was estimated to be about 17 mL (*19*). Sampling of a large amount of blood may affect the physiologic condition of the rats. In the present study, only 0.2 mL of arterial blood was taken at each measurement, and the total volume of blood withdrawn was 0.5 mL. This volume was much smaller than that reported in previous studies (*9,20*). The small-volume sampling in this study was considered to have a negligible influence on systemic circulation.

We measured the radioactivity of whole blood and plasma, weighing around 0.025 g, by well counter to examine the volume dependency of the radioactivity count. It was confirmed that the measurement was accurate and that reproducibility was feasible for 0.025-g samples.

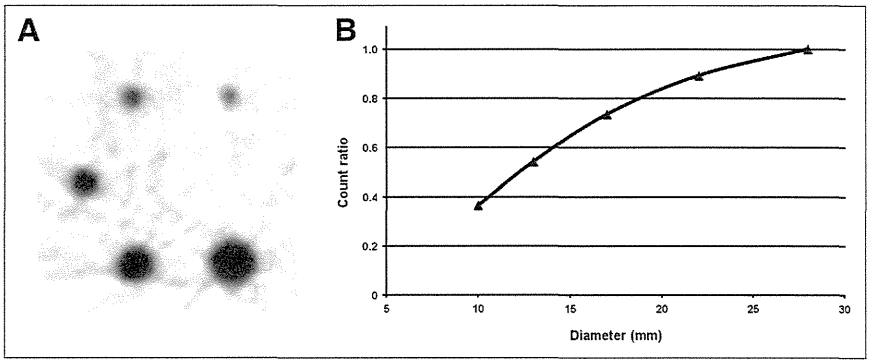

FIGURE 2. PET image of NEMA phantom (A) and curve constructed by plotting mean count ratios against sphere diameters (B).

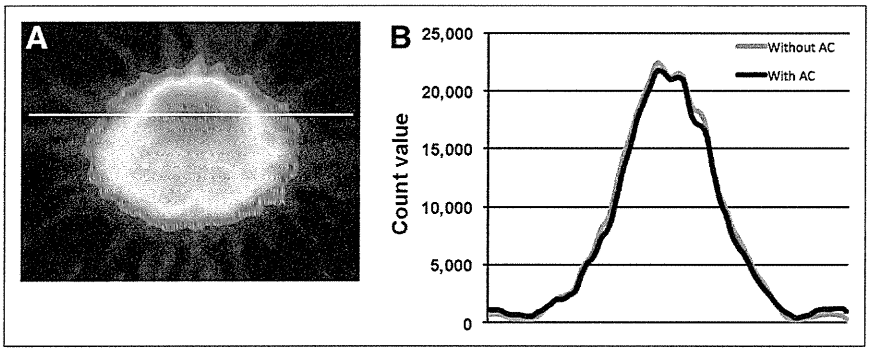

FIGURE 3. ^{15}O-O_2 PET image of brain (white line indicates location of profile curves) (A) and profile curves of brain with and without attenuation correction (B). AC = attenuation correction.

In previous studies, tissue attenuation of ^{15}O was corrected by means of transmission data acquired using the external rod source of ^{68}Ge–^{68}Ga (*9*). The scan duration ranged from 30 to 60 min. When we performed a transmission scan, the duration of the total PET experiment almost doubled from 70 to 130 min. Furthermore, making tissue attenuation maps of small animals using a clinical PET device increases transmission bias and noise because of the large ring diameter. Underestimation by 4% was observed in the experimental study of a rat phantom of 3-cm diameter without attenuation correction, as reported in the previous study (*21*). Scatter fraction in the 2D mode was 13% in the human study according to the performance of our PET scanner (*13*). In our study, we could not perform attenuation and scatter correction because of the limitation of the PET scanner. However, we confirmed from our experimental studies that the tissue attenuation in the rat head and the scatter fraction from outside the brain were small. The fact that attenuation and scatter correction needed to be performed to improve the accuracy was a limitation of our study.

We monitored the systemic BP, body temperature, heart rate, hemoglobin concentration, $PaCO_2$, PaO_2, and SaO_2. Among these parameters, the PaO_2 (56.3 ± 9.3 mm Hg) was unexpectedly lower than the physiologic range and variable, compared with the other physiologic measurements. One possible reason was the slightly reduced oxygen concentration of the inhaled gas. The oxygen concentration of the gas from the radioactive gas stabilization system was 18.1% in ^{15}O-O_2 gas studies. In the target box for ^{15}O-O_2 production, the concentration ratio of cold O_2 to N_2 was 0.5%/99.5%. The ^{15}O-O_2 gas with N_2 gas from the target box was transferred to the gas stabilizer system, and room air was mixed with the ^{15}O-O_2 gas while radioactivity concentration was adjusted. As a result, the oxygen concentration of the inhaled gas was lower than that of the room air because of the addition of the target gas, in which the main component was N_2 gas. Another reason was the effect of the anesthesia used in this study. Reduction in the PaO_2 after the administration of butorphanol, buprenorphine, and midazolam was reported from a previous rabbit study, and this effect was sustained for about 2 h (*22*). High variability in the PaO_2 was probably due to the differences in individual reactions to the anesthesia. To maintain physiologic conditions and reduce the variability, the constitution of the inhaled gas should be readjusted by the addition of O_2.

In previous PET studies, a bolus injection of ^{15}O-labeled water (^{15}O-H_2O) was used for quantitative measurement of the CBF; the reported CBF values ranged from 35 to 51 mL/100 g/min (*6,8,20*). Kobayashi et al. reported a steady-state method consisting of a bolus injection followed by injection of ^{15}O-H_2O at slowly increasing doses with a multiprogramming syringe pump (*9*). The CBF value under chloral hydrate anesthesia was 49.2 ± 5.4 mL/100 g/min. The CBF value measured in our study was much smaller than these previously reported values. The first possible reason is underestimation due to the partial-volume effect. We used a clinical PET device with a larger spatial resolution (4.0 mm in FWHM). According to the phantom study, this underestimation was by approximately 70%, because the diameter of the rat brain is about 15 mm. The radioactivity

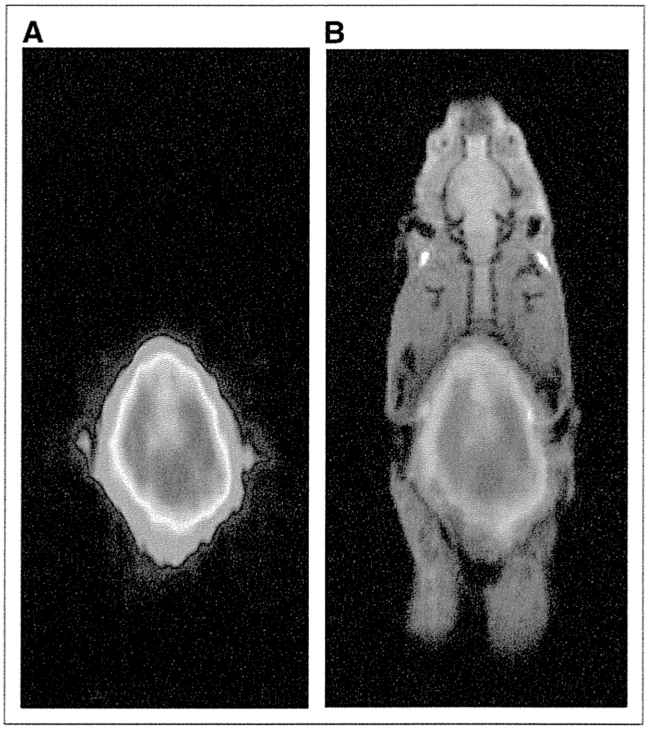

FIGURE 4. Coronal PET (A) and PET/MR (B) images of lung phantom ventilated with ^{15}O-O_2 gas.

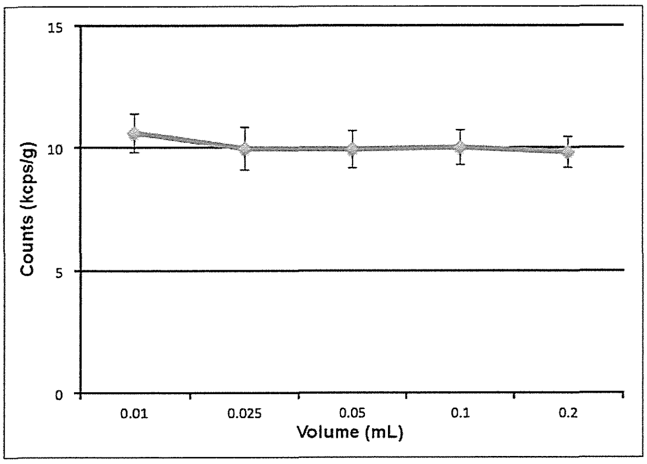

FIGURE 5. Relationship between radioactivity (kcps/g) and sample volume of $H_2{}^{15}O$ solution by well counter.

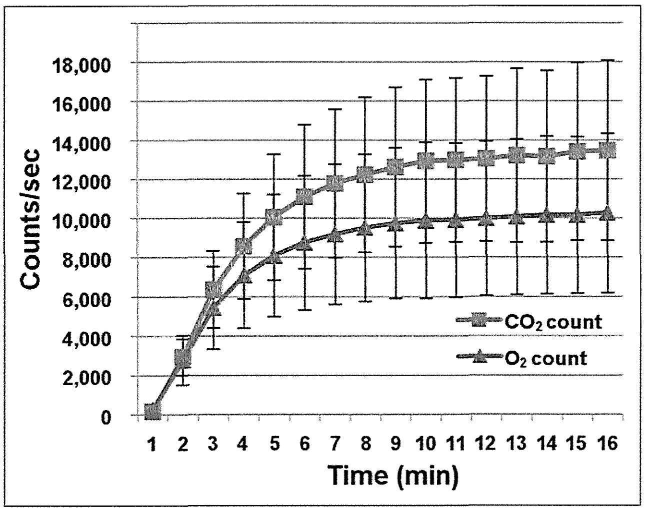

FIGURE 6. Time–activity curves in brain during continuous inhalation of ^{15}O-CO_2 and ^{15}O-O_2 gas. cps = count/s.

count in the brain was divided by 0.70 to correct the partial-volume effect for full count recovery. This corrected count was substituted for C_t in the following equation described in the "Methods" section: regional CBF = $\lambda/(C_a/C_t - 1/\rho)$. After correction for the partial-volume effect, we obtained a whole-brain CBF value of approximately 84 mL/100 mL/min, which is in agreement with the values obtained by the autoradiographic method (*16*) and the Kety–Schmidt method (*23,24*), the results of which are not influenced by the partial-volume effect. The second possible reason is the influence of anesthesia. Most previous studies used chloral hydrate, which is difficult to use because of its narrow margin of safety and lack of analgesic effect. The different anesthetic technique used might also have produced the differences in the results. The third reason is the influence of $PaCO_2$ on the CBF. Hypocapnia causes reduction of the global CBF in the rat under isoflurane or halothane anesthesia (*25*). On the basis of studies using the steady-state method, Kobayashi et al. reported that the CBF was 49.2 ± 5.4 mL/100 g/min when the $PaCO_2$ was 49.7 ± 3.9 mm Hg (*9*). In this study, the CBF was 32.3 ± 4.5 mL/100 mL/min when the $PaCO_2$ was 36.6 ± 1.6 mm Hg. The lower CBF value in the present study was partly due to the lower $PaCO_2$ levels. Another possible reason is that systemic underestimation by the steady-state inhalation method, compared with that in the bolus injection method, was partly due to the tissue heterogeneity between the gray and white matter (*26*).

TABLE 1
BP, HR, and Arterial Blood Gas Data During PET Measurement

Parameter	Mean ± SD
BP (mm Hg) (*n* = 4)	
Systolic	106 ± 4
Diastolic	79 ± 5
HR (bpm) (*n* = 4)	326 ± 20
pH	7.45 ± 0.03
$PaCO_2$ (mm Hg)	36.6 ± 1.6
PaO_2 (mm Hg)	56.3 ± 9.3
SaO_2 (%)	89.3 ± 3.7

Few PET studies have reported measurement of OEF. Reported values of OEF in rats under pentobarbital anesthesia are 54% ± 11% using the kinetic method with injectable ^{15}O-O_2 and 57% ± 13% using the surgical method based on the arterial–venous difference in oxygen concentration (*4,20*). Other studies using ^{15}O-O_2 hemoglobin–containing liposome vesicles reported OEF values in rats under chloral hydrate anesthesia of 61% ± 16% (6) and 56% ± 4% (*27*). OEF is a function of the ^{15}O-O_2/^{15}O-CO_2 count ratio. OEF is not significantly affected by the partial-volume effect, because the calculation involves canceling out by dividing the ^{15}O-O_2 count by the ^{15}O-CO_2 count in the brain tissue. The OEF value calculated in our study was a little higher than the previously reported values. The OEF values reported from other studies were also higher than those reported from human studies. The OEF values were 54%–61% in the normal rat study but only 44% in a normal human study (*28*). Previous studies reported higher OEF values in monkeys (54% ± 6%) and pigs (59% ± 9%) (*29,30*). Therefore, differences among species might be the reason for the high OEF in the rats in the present study. OEF elevation was observed in the MCA occlusion model, as in the human brain in our study. The OEF values were 74.3% and 65.4% in the ipsilateral and contralateral MCA territories, respectively. The capacity to adapt to flow decreases was observed in rats, just as in humans.

Yee et al. reported quantitative measurement of $CMRO_2$ in the rat brain with briefly inhaled ^{15}O-labeled oxygen gas (*3*). The measured $CMRO_2$ value under α-chloralose anesthesia was 6.65 ± 0.48 mL/100 g/min. Temma et al. used an artificial lung to dissolve ^{15}O-O_2 in the blood and reported a $CMRO_2$ value of 4.3 ± 1.3 mL/100 g/min under pentobarbital anesthesia (*20*). Another group used hemoglobin-containing liposome vesicles or liposome-encapsulated hemoglobin with ^{15}O-O_2 and reported $CMRO_2$ values of 6.8 ± 1.4 (under chloral

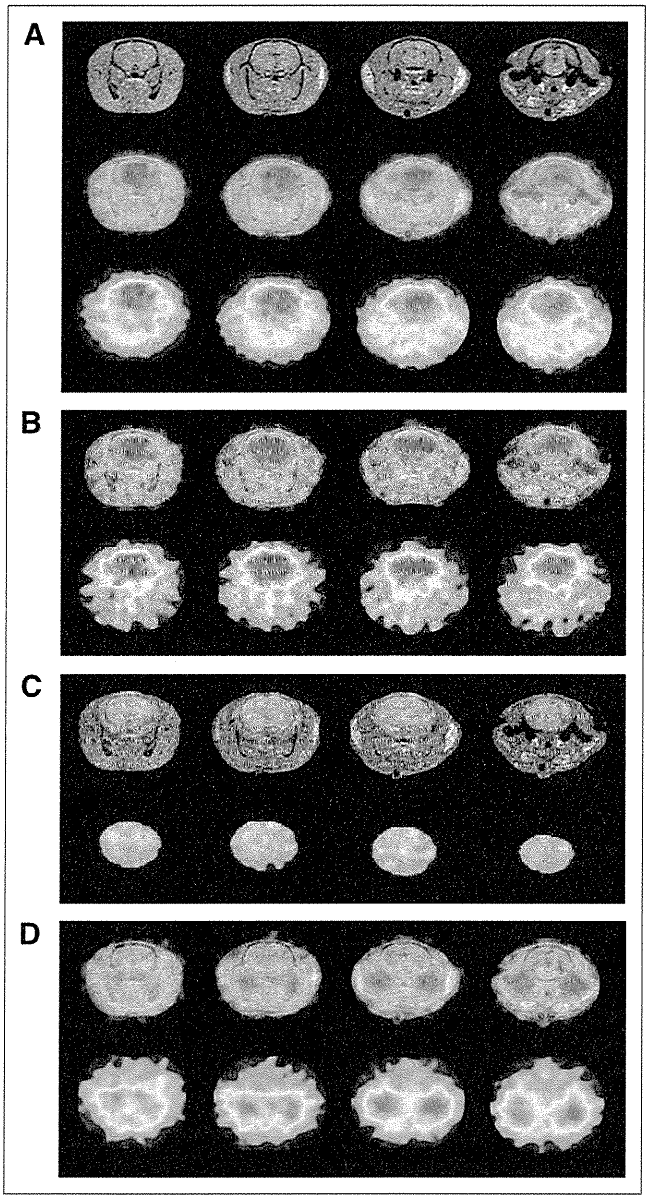

FIGURE 7. MR (upper), PET/MR fusion (middle), and PET (lower) images of CBF (A). PET/MR fusion (upper) and PET (lower) images of CMRO2 (B), OEF (C), and CBV (D). Images in same column indicate same transaxial cross-section of brain (A–D).

hydrate anesthesia) and 4.8 ± 0.2 mL/100 g/min (under ketamine and xylazine anesthesia), respectively (*6,7*). Kobayashi et al. recently reported a $CMRO_2$ value of 6.2 ± 0.4 mL/100 g/min under chloral hydrate anesthesia as measured by the steady-state method with injection of $^{15}O_2$ hemoglobin–containing vesicles (*27*). The $CMRO_2$ value measured in our study (3.23 ± 0.42 mL/100 mL/min) was smaller than these previously reported values. However, after correction for the partial-volume effect, the $CMRO_2$ was approximately 8.4 mL/100 mL/min, which is in agreement with the values (10.3 and 7.57 mL/100 mL/min) obtained by the method of Kety and Schmidt (*23,24*).

There have been no reports of measurement of the CBV in the rat brain by ^{15}O-CO gas inhalation PET. This study evaluated all PET parameters (CBF, $CMRO_2$, OEF, and CBV) by ^{15}O-labeled gases with correction for intravascular hemoglobin-bound $^{15}O_2$. Kobayashi reported a mean value of the CBV of 4.9 ± 0.4 mL/100 g as measured by injection of ^{15}O-CO hemoglobin–containing vesicles, consistent with the result of our study (*27*). The small-vessel–to–large-vessel hematocrit ratio in the rat brain has been fixed at 0.70 (*17*); this ratio was shown to have little effect on the OEF or $CMRO_2$ values. When we used 0.85 as the value of the hematocrit ratio (a value often used in clinical studies), the $CMRO_2$ and OEF increased by approximately 1% (data not shown).

Quantitative PET measurement in a rat model of unilateral MCA occlusion was performed as an experimental study. A decrease in both the CBF and the $CMRO_2$ and an increase in the OEF were detected in the ipsilateral MCA territory (data not shown). We concluded that evaluation in an ischemia model is feasible with this PET technique.

CONCLUSION

Although further improvements of the gas inhalation system may be needed, we demonstrated the feasibility of quantitative measurements of CBF, CBV, $CMRO_2$, and OEF using PET according to the original steady-state inhalation method of $^{15}O\text{-}CO_2$ and $^{15}O\text{-}O_2$ gas and the CBV measurement by ^{15}O-CO gas inhalation in normal rats under anesthesia.

DISCLOSURE

The costs of publication of this article were defrayed in part by the payment of page charges. Therefore, and solely to indicate this fact, this article is hereby marked "advertisement" in accordance with 18 USC section 1734. This study was partly supported by the Molecular Imaging Program, a grant (no. 21591561) from the Ministry of Education, Culture, Sports, Science, and Technology (MEXT), Japan. No other potential conflict of interest relevant to this article was reported.

REFERENCES

1. Fox PT, Mintun MA, Raichle ME, Miezin FM, Allman JM, Van Essen DC. Mapping human visual cortex with positron emission tomography. *Nature.* 1986;323:806–809.
2. Powers WJ, Clarke WR, Grubb RL Jr, Videen TO, Adams HP Jr, Derdeyn CP. Extracranial-intracranial bypass surgery for stroke prevention in hemodynamic cerebral ischemia: the Carotid Occlusion Surgery Study randomized trial. *JAMA.* 2011;306:1983–1992.
3. Yee SH, Lee K, Jerabek PA, Fox PT. Quantitative measurement of oxygen metabolic rate in the rat brain using microPET imaging of briefly inhaled ^{15}O-labelled oxygen gas. *Nucl Med Commun.* 2006;27:573–581.
4. Magata Y, Temma T, Iida H, et al. Development of injectable O-15 oxygen and estimation of rat OEF. *J Cereb Blood Flow Metab.* 2003;23:671–676.
5. Temma T, Magata Y, Kuge Y, et al. Estimation of oxygen metabolism in a rat model of permanent ischemia using positron emission tomography with injectable15O-O2. *J Cereb Blood Flow Metab.* 2006;26:1577–1583.
6. Tiwari VN, Kiyono Y, Kobayashi M, et al. Automatic labeling method for injectable ^{15}O-oxygen using hemoglobin-containing liposome vesicles and its application for measurement of brain oxygen consumption by PET. *Nucl Med Biol.* 2010;37:77–83.
7. Awasthi V, Yee SH, Jerabek P, Goins B, Phillips WT. Cerebral oxygen delivery by liposome-encapsulated hemoglobin: a positron-emission tomographic evaluation in a rat model of hemorrhagic shock. *J Appl Physiol.* 2007;103:28–38.

8. Weber B, Spath N, Wyss M, et al. Quantitative cerebral blood flow measurements in the rat using a beta-probe and H2 ^{15}O. *J Cereb Blood Flow Metab.* 2003; 23:1455–1460.
9. Kobayashi M, Kiyono Y, Maruyama R, Mori T, Kawai K, Okazawa H. Development of an $H_2{}^{15}O$ steady-state method combining a bolus and slow increasing injection with a multiprogramming syringe pump. *J Cereb Blood Flow Metab.* 2011;31:527–534.
10. Jones T, Chesler DA, Ter-Pogossian MM. The continuous inhalation of oxygen-15 for assessing regional oxygen extraction in the brain of man. *Br J Radiol.* 1976; 49:339–343.
11. Frackowiak RS, Lenzi GL, Jones T, Heather JD. Quantitative measurement of regional cerebral blood flow and oxygen metabolism in man using ^{15}O and positron emission tomography: theory, procedure, and normal values. *J Comput Assist Tomogr.* 1980;4:727–736.
12. Lammertsma AA, Jones T. Correction for the presence of intravascular oxygen-15 in the steady-state technique for measuring regional oxygen extraction ratio in the brain: 1. Description of the method. *J Cereb Blood Flow Metab.* 1983;3:416–424.
13. Iida H, Miura S, Kanno I, Ogawa T, Uemura K. A new PET camera for noninvasive quantitation of physiological functional parametric images: Headtome-V-Dual. In: Myers R, Cunningham V, Bailey D, Jones T, eds. *Quantitation of Brain Function Using PET.* San Diego, CA: Academic Press; 1996:57–61
14. Yamamoto S, Imaizumi M, Kanai Y, et al. Design and performance from an integrated PET/MRI system for small animals. *Ann Nucl Med.* 2010;24:89–98.
15. Shimamura N, Matchett G, Tsubokawa T, Ohkuma H, Zhang J. Comparison of silicon-coated nylon suture to plain nylon suture in the rat middle cerebral artery occlusion model. *J Neurosci Methods.* 2006;156:161–165.
16. Herscovitch P, Raichle ME. What is the correct value for the brain–blood partition coefficient for water? *J Cereb Blood Flow Metab.* 1985;5:65–69.
17. Cremer JE, Seville MP. Regional brain blood flow, blood volume, and haematocrit values in the adult rat. *J Cereb Blood Flow Metab.* 1983;3:254–256.
18. Ibaraki M, Miura S, Shimosegawa E, et al. Quantification of cerebral blood flow and oxygen metabolism with 3-dimensional PET and ^{15}O: validation by comparison with 2-dimensional PET. *J Nucl Med.* 2008;49:50–59.
19. Lee HB, Blaufox MD. Blood volume in the rat. *J Nucl Med.* 1985;26:72–76.
20. Temma T, Kuge Y, Sano K, et al. PET O-15 cerebral blood flow and metabolism after acute stroke in spontaneously hypertensive rats. *Brain Res.* 2008;1212:18–24.
21. Chow PL, Rannou FR, Chatziioannou AF. Attenuation correction for small animal PET tomographs. *Phys Med Biol.* 2005;50:1837–1850.
22. Schroeder CA, Smith LJ. Respiratory rates and arterial blood-gas tensions in healthy rabbits given buprenorphine, butorphanol, midazolam, or their combinations. *J Am Assoc Lab Anim Sci.* 2011;50:205–211.
23. Hägerdal M, Harp J, Nilsson L, Siesjo BK. The effect of induced hypothermia upon oxygen consumption in the rat brain. *J Neurochem.* 1975;24:311–316.
24. Nilsson B, Siesjo BK. A method for determining blood flow and oxygen consumption in the rat brain. *Acta Physiol Scand.* 1976;96:72–82.
25. Young WL, Barkai AI, Prohovnik I, Nelson H, Durkin M. Effect of PaCO2 on cerebral blood flow distribution during halothane compared with isoflurane anaesthesia in the rat. *Br J Anaesth.* 1991;67:440–446.
26. Herscovitch P, Raichle ME. Effect of tissue heterogeneity on the measurement of cerebral blood flow with the equilibrium C15O2 inhalation technique. *J Cereb Blood Flow Metab.* 1983;3:407–415.
27. Kobayashi M, Mori T, Kiyono Y, et al. Cerebral oxygen metabolism of rats using injectable ^{15}O-oxygen with a steady-state method. *J Cereb Blood Flow Metab.* 2012;32:33–40.
28. Ito H, Kanno I, Kato C, et al. Database of normal human cerebral blood flow, cerebral blood volume, cerebral oxygen extraction fraction and cerebral metabolic rate of oxygen measured by positron emission tomography with ^{15}O-labelled carbon dioxide or water, carbon monoxide and oxygen: a multicentre study in Japan. *Eur J Nucl Med Mol Imaging.* 2004;31:635–643.
29. Kudomi N, Hayashi T, Teramoto N, et al. Rapid quantitative measurement of CMRO(2) and CBF by dual administration of (15)O-labeled oxygen and water during a single PET scan-a validation study and error analysis in anesthetized monkeys. *J Cereb Blood Flow Metab.* 2005;25:1209–1224.
30. Mörtberg E, Cumming P, Wiklund L, Rubertsson S. Cerebral metabolic rate of oxygen (CMRO2) in pig brain determined by PET after resuscitation from cardiac arrest. *Resuscitation.* 2009;80:701–706.

Microvascular Research 84 (2012) 178–187

Contents lists available at SciVerse ScienceDirect

Microvascular Research

journal homepage: www.elsevier.com/locate/ymvre

Image-based vessel-by-vessel analysis for red blood cell and plasma dynamics with automatic segmentation

Hiroshi Kawaguchi [a], Kazuto Masamoto [a,b,*], Hiroshi Ito [a], Iwao Kanno [a]

[a] *Molecular Imaging Center, National Institute of Radiological Sciences, 4-9-1 Anagawa, Inage, Chiba 263-8555, Japan*
[b] *Center for Frontier Science and Engineering, University of Electro-Communications, 1-5-1 Chofugaoka, Chofu, Tokyo 182-8585, Japan*

ARTICLE INFO

Article history:
Accepted 1 May 2012
Available online 12 May 2012

ABSTRACT

The aim of the present study was to test the hypothesis that vascular tones of cortical surface and parenchymal blood flow can be dissociated depending on the perturbation. To this end, a novel image-based analytical method for quantitatively measuring vessel diameters and flow dynamics was developed. The algorithm relies on the spatiotemporal coherence of the pixel intensity changes induced by the transit of the fluorescent signals measured using confocal laser scanning fluorescent microscopy in the rat cerebral cortex. A cocktail of fluorescently labeled red blood cell (RBC) and plasma agents was administered to simultaneously compare RBC and plasma dynamics in the same vascular networks. The time to fluorescent signal appearance and the width of the fluorescent signal were measured in each segment and compared between sodium nitroprusside-induced global and sensory stimulation-induced local perturbation conditions. We observed that infusion of sodium nitroprusside induced significant vasodilation in the surface artery, particularly in the small arteries (1.8-fold increase). Vasodilation induced by sensory stimulation was observed to depend on vessel size, but significant changes were only detected for the small arteries and veins. Measurements of the time to venous appearance revealed that appearance time was extended by sodium nitroprusside, but shortened during forepaw stimulation, relative to the control condition. Both perturbations provoked the largest changes between the small artery and vein segments, indicating that the changes in the appearance time originate from blood passage through parenchymal microcirculation. These findings support the hypothesis that cortical surface vascular tone and parenchymal blood flow are individually coordinated.

© 2012 Elsevier Inc. All rights reserved.

Introduction

It is well known that the network structure of the cerebral vasculature differs between the cortical surface and parenchymal tissue (Mchedlishvili, 1986). On the surface, arteries have mesh-like anastomosis (i.e., arterio-arterial anastomosis), but no capillaries are present (Schaffer et al., 2006). In the parenchyma, each arteriole forms a terminal arteriole that governs a unit of microvascular networks (Nishimura et al., 2007), and capillary density roughly matches metabolic activity of glucose in the region (Borowsky and Collins, 1989). These morphological features have been thought to play a critical role in coordinating the spatial balance of blood flow supply to meet the localization of the brain functions (i.e., region-specific demand).

It has been proposed that the cortical surface arteries have a major role in controlling the parenchymal blood flow (Mchedlishvili, 1986; Rosenblum and Kontos, 1974). This view was supported by the findings of the parallel changes in parenchymal blood flow and vascular tone of cortical surface arteries during both systemic perturbations induced with an inhalation of 5% carbon dioxide in air and systemic hypertension (Haberl et al., 1989a). However, a dissociation of the surface artery and parenchymal blood flow responses were also found for perturbation induced with topically applied vasoactive agents (Haberl et al., 1989b). These findings indicate that different blood flow regulation mechanisms may exist depending on global and local perturbation.

To test the hypothesis that vascular tone of cortical surface and parenchymal blood flow can be dissociated depending on the perturbation, the present study developed a novel image-based analytical method with high-speed laser scanning confocal microscopy. The algorithm relies on the spatiotemporal coherence of the pixel intensity changes induced by a transit of the fluorescent agents through the time-lapse images captured on the cortical surface of the rats (Autio et al., 2011). To further determine the detailed microcirculation properties, a cocktail of fluorescently labeled red blood cell (RBC) and quantum dot (Qdot) as a plasma marker was administered. The individual vessel widths and transit times of the both RBC and plasma signals were then determined to characterize their vessel-by-vessel

---

[*] Corresponding author at: Center for Frontier Science and Engineering, University of Electro-Communications, 1-5-1 Chofugaoka, Chofu, Tokyo 182-8585, Japan. Fax: +81 42 443 5930.
E-mail address: masamoto@mce.uec.ac.jp (K. Masamoto).

0026-2862/$ – see front matter © 2012 Elsevier Inc. All rights reserved.
doi:10.1016/j.mvr.2012.05.001

responses to either systemic global or local perturbations induced with intravenous administration of sodium nitroprusside (SNP) or with electrical forepaw stimulation, respectively.

Materials and methods

Animal preparation

The protocols of all animal experiments were approved by the Institutional Animal Care and Use Committee, and all experiments were carried out in accordance with the institutional guidelines for conducting of animal experiments. A total of five male Sprague–Dawley rats (7–9 weeks, 270–340 g) were used for the experiments. Each animal was initially anesthetized with isoflurane (4–5% for induction and 1.8–2.2% for surgery), and intubation was performed for mechanical ventilation. Three catheters were inserted in the femoral artery, femoral vein, and external carotid artery for systemic arterial blood pressure monitoring and blood sampling, drug infusion, and administration of fluorescent agents, respectively. Each anesthetized animal was secured with a stereotactic apparatus (SG-3N, Narishige, Tokyo, Japan), and the skull over the somatosensory area (3 mm by 3 mm) was removed (Park et al., 2008). The dura was also thinned to enhance translucency, but a thin layer was preserved to maintain cortical microcirculation homeostasis. The exposed cortex was then covered with warmed saline.

After all surgery was completed, the isoflurane concentration was reduced to 1.3–1.5% (Masamoto et al., 2007), and the animal's condition was stabilized for 1 h prior to the measurements. The respiration rate was fixed at 0.87 Hz, and the ventilatory volume was adjusted to maintain end-tidal CO_2 levels (35–42 mm Hg) and blood gas conditions ($PaO_2 = 128 \pm 25$ mm Hg, $PaCO_2 = 35 \pm 3$ mm Hg, $pH = 7.40 \pm 0.09$, $Hct = 42 \pm 2\%$). The end-tidal gas and arterial blood gas conditions were measured with a capnograph monitor (V9400, Smiths Medical PM, Inc., Norwell, MA) and a blood gas analyzer (i-STAT 300F Analyzer, i-STAT Corporation, East Windsor, NJ), respectively. Body temperature, measured rectally, was maintained at 37 °C with a heating pad (TR-200, Fine Science Tools Inc., Foster City, CA).

Time-lapse imaging

A cocktail of Qdot 605 (1 μM in stock solution with saline, Invitrogen, San Diego, CA) and fluorescently-labeled RBCs that were collected from a donor rat and incubated with fluorescein isothiocyanate (FITC) (Seylaz et al., 1999), was injected using syringe pump (PHD4400, Harvard Apparatus, MA) into the external carotid artery at a rate of 2.2 mL/min with an injection volume of 0.02 mL (i.e., about 0.5-s duration for one-shot injection) in which hematocrit level was preliminarily adjusted to be within physiologic limits. A previous study has shown this type of water-soluble Qdot (negatively charged) can be used as an analogous agent to the conventionally used fluorescent dextrans (Larson et al., 2003). Thus, we assumed that Qdot represents plasma flow. Images were captured at the cortical surface with a laser scanning confocal microscope (TCS SP5, Leica Microsystems Gmbh, Wetzlar, Germany) with a 5× objective lens (PL FLUOTAR 0.12 NA, Leica Microsystems Gmbh, Wetzlar, Germany). The excitation light was 488 nm Argon, while the emission signal was detected with two photomultiplier tubes (R6357, Hamamatsu Photonics KK., Hamamatsu, Japan) for simultaneous detection of FITC-RBC and Qdot-plasma through an emission filter of 545/90 nm and 605/20 nm, respectively. For Qdot detection channel, a narrow spectrum emission filter was set and the gain level of the detector was adjusted to minimize potential contamination of the signals from FITC which has a relatively broad emission spectrum (480 to 620 nm at 5% of the peak). The size of each single plane image was 512 by 512 pixels (field of view: 1.82 mm by 1.82 mm), and fast time-lapse imaging was performed at a frame rate of 14.2 fps (i.e., 70.4-ms interval for onset to onset) with a total acquisition time of 18 s (256 frames). Due to the low numerical aperture of the lens, the resolution in the depth direction was approximately 50 μm and the lateral resolution was approximately 3 μm under our experimental conditions.

Global and local perturbation

Global perturbation was induced with an intravenous injection of sodium nitroprusside (SNP; 2.2 mg/kg body weight), a well-known vasodilator (Auer, 1978). After blood pressure was stabilized (40 to 50 mm Hg) following the SNP injection, time-lapse imaging was initiated. Previous studies have confirmed that under these ranges of systemic blood pressure, evoked neural activity and oxygen metabolic rate are preserved, and only the evoked vascular response is suppressed (Fukuda et al., 2006; Masamoto et al., 2008).

Local perturbation was given by electrical pulse stimuli (1.0 ms width and 1.5–1.7 mA current with 6 Hz frequency for 25 s) to the forepaw via two needles implanted under the skin in the contra-lateral side of the measurement (Kim et al., 2010; Masamoto et al., 2007). The active area was preliminarily identified by measuring the area of arterial dilation responding to forepaw stimulation. The measurements were started 5 s after the onset of forepaw stimuli, when the evoked hemodynamic changes were observed to reach a plateau.

In each perturbation experiment, between one and four measurements were repeatedly conducted, and a total of four to nine measurements were performed in each animal. In these experiments, mean arterial blood pressure was 97 ± 11 and 45 ± 1 mm Hg under control and SNP conditions, respectively ($N = 3$ animals), and 93 ± 3 and 94 ± 3 mm Hg under control and forepaw stimulation conditions, respectively ($N = 3$ animals).

Measurement of appearance and disappearance times

Image analysis was performed with custom-written software (MATLAB, The Mathworks, Natick, MA) after all images were transferred to a computer workstation. First, the times of appearance and disappearance of the fluorescent agent were determined on a per-pixel basis. Since the original raw images involved shot noises from the photomultiplier tube, temporal smoothing was performed every 5 frames on each pixel's raw data. The mean and standard deviation of the baseline intensity were calculated for several tens of frames obtained from the beginning of the measurement. The appearance time was determined as the earliest time point where the pixel intensity surpassed the mean + 3SD of the baseline intensity. Similarly, the disappearance time, the latest time point where the intensity decreased to baseline, was determined by applying the same pixel intensity criterion to the data with time reversed (so that the end became the beginning). For the original (non-reversed) data, the temporal origin ($t = 0$) was set at the earliest time point in the image for the appearance of the plasma agent measured under control conditions.

Automatic segmentation

In imaging analysis, a minimum unit can be a single pixel; however, pixel-to-pixel comparison is not valid for images containing displacement of the signal location, such as during vasodilation or vasoconstriction. This study instead used a single vessel segment as a minimum unit, which overcomes this limitation for comparing images obtained at different conditions. First, an extraction of the vessel area was made by determining appearance time measured for all 512 by 512 pixels in the image. If the appearance time was assigned as null, the pixel was regarded as being in the non-vessel area (i.e., tissue area). Second, the vessel area was divided into either artery or vein clusters, based on the differences of their appearance time. A histogram of the appearance time typically showed a bimodal distribution (i.e., originating from artery and vein differences). However, this does not necessarily mean that the pixels showing the earlier appearance time were all belong to artery components and vice versa (e.g., for the smallest artery and vein components). Thus, the present study focused on the spatiotemporal continuity of the signal appearance within and among the connecting vessels to achieve a complete separation of the artery and vein segments. To this end, an iterative region-growing procedure was applied to cluster similar appearance time areas into the respective large artery and vein areas which showed two predominant components in the histogram of appearance time. The vessel area was first subdivided into 8 components whose appearance time was identical. Then, the components were organized in ascending order according to their size (i.e., number of pixels), and the component that had the smallest size was merged into the adjacent component that had the closest appearance time. If there were several candidates that had equally close appearance time, the largest component among the candidates was selected. Then, the appearance time in the smallest component was replaced to that of the merged component, and the histogram of appearance time was updated. These iterations were repeated until two separate clusters (i.e., artery and vein compartments) appeared in the histogram. Finally, the cluster that had the earlier appearance time was assigned as an artery area, and another cluster was assigned as a vein area. Based on these clustering methods, the vessel area was segmented and the separation of artery and vein segments was visually confirmed by comparing the segmented image with the original raw image.

If necessary, the manual correction was made for artery and vein segmentation. For example, an intersection of the artery and vein caused discontinuous vessel segmentation. In the case of a vein apparently crossing over an artery, the edges of venous segments along the intersection were invaded by arterial signals that passed under the venous trunk because of low absorption effects near the side of the vein. To correct this error, the two discontinuous portions of the arterial segment were manually connected to recover the artery segments lost under the vein segment. If the artery crossed over a vein, the discontinuous vein segment was present in the appearance time image. Because the crossing area was a mixture of the artery and vein appearance time signals, the lost portions of the venous segments were recovered based on the disappearance time image. Alternatively, the mixed signals of the arterial and venous components in these crossing areas can be deconvoluted into the original arterial and venous signals, if a whole time-course of the fluorescent signals was available and the both signals from connecting arteries and veins to the crossing areas were detectable. However, due to a lack of the whole time-course data, only manual correction for segmentation was made possible, but no further analysis for these crossing areas was made in the present study.

The last step of the segmentation procedure was to define a single vessel segment which had two branches at both ends. First, artery and vein images were thinned in the longitudinal direction of the vessel tree. Then, the thinned vessels were segmented with a part-type segmentation method for articulated voxel shapes (Reniers et al., 2008) with modifications for two-dimensional images. To determine the branching pattern of the vessel, a geodesicness measure (γ) was computed at each pixel on the vessel segments except for the junctions and endpoints (Reniers et al., 2008). For example, if the target segment vessels had a high geodesicness measure (e.g., $\gamma =$ nearly 1), those vessels were judged as running in parallel to the vessel wall and thus defined as a single segment. If their geodesicness was low (e.g., $\gamma = 0.5$–0.8), the vessels were considered as two separate vessels (i.e., two segments) (see also Supplemental Fig. S1 which represent the results of segmentation from the raw image shown in Fig. 1a). These segmentation tools we made are disclosed in Matlab Central (http://www.mathworks.com/matlabcentral/fileexchange/36031-vessel-branch-segmentation).

Measurement of passage width

The width of the vessel segment, i.e., the spatial width of the contrast agent's passage, was measured in each vessel segment. First, a Euclidean distance technique was applied for all segmented vessels to measure the gross distance from the edge of the vessel segment to the thinned vessels along the longitudinal direction of the vessel segment. Then, the mean of the largest 5% of distances (i.e., the farthest points from the edge of the vessel wall) was measured and doubled to compute the width. Also, the area of the segmentalized vessels was measured and represented by the number of pixels. Finally, each vessel segment was indexed with an identical number across different imaging sessions, i.e., control, global (SNP), and local (forepaw) perturbation in each animal, by referring to a plasma flow image obtained under control conditions. Then, all vessel segments were sorted into 6 categories by referencing the width of the plasma passage (i.e., the lumen diameter): small (SA; $<25\,\mu m$), medium (MA; >25, $<50\,\mu m$), and large arteries (LA; $>50\,\mu m$), and small (SV, $<50\,\mu m$), medium (MV, >50, $<100\,\mu m$) and large veins (LV, $>100\,\mu m$).

Statistics

Statistical analysis was performed using custom MATLAB scripts. A Student's t-test was applied to evaluate the changes in diameter and appearance time between control and perturbation conditions for each vascular segment. Bonferroni corrections were performed for comparisons among 6 vascular segments. A p-value of less than 0.05/6 was considered statistically significant. Data were represented as mean ± standard deviation.

Results

Imaging the spatiotemporal evolution of fluorescent agents

Time-lapse images of the fluorescent agents showed distinct differences between the fluorescent signal changes in artery and vein compartments (Fig. 1a). The apparently similar spatiotemporal behaviors were seen for the RBC and plasma markers (Fig. 1a). The changes in signal intensity were sufficient to determine both appearance and disappearance times on a single-pixel basis after removal of shot noises (Fig. 1b). However, due to a limited dynamic range, the peak intensity was not measurable in our experimental condition (i.e., a lack of a whole time–intensity curve). The reconstructed images for both appearance and disappearance times showed detailed spatiotemporal evolution of the injected fluorescent agents within and across the vascular networks (Figs. 1c and d).

In arterial compartments, relatively uniform appearance and disappearance times were seen for all vessel sizes. In contrast, the veins showed different patterns depending on the size of the vessels. Small veins had a relatively homogeneous pattern and fast appearance and disappearance times, whereas medium and large veins showed a stripe pattern of passage times that continued from their individual daughter veins along the vessel wall. In these vessels, the stripe patterns were observed to be unmixed in a radial direction within the vessel segment, indicating a parallel flow.

Automatic segmentation and representative histogram

The spatiotemporal continuity of the fluorescent signal dynamics was used for automated segmentation of the artery and vein

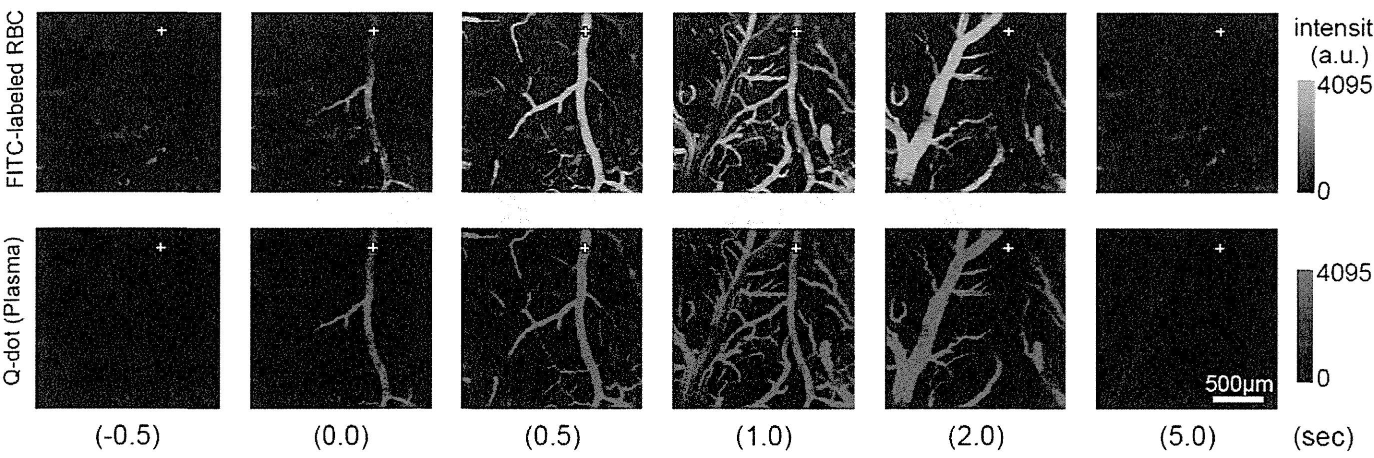

(a) typical time frames from a raw time-lapse images

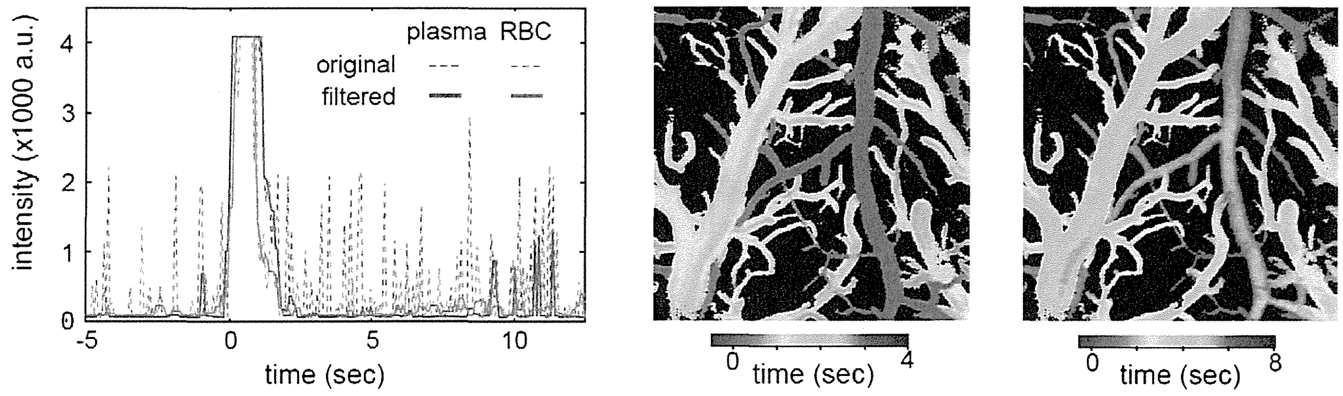

(b) time series of a pixel (c) appearance time (d) disappearance time

Fig. 1. Imaging and measurement of spatiotemporal fluorescent signal changes. (a) Representative time-lapse images for the transit of FITC-labeled RBC (green, upper) and Qdot plasma markers (red, bottom) measured using confocal laser scanning microscopy in the rat cerebral cortex. The fluorescent agents first appeared in the artery (time 0) and then propagated to the small to large veins. No detectable differences were seen between the RBC and plasma dynamics. (b) Time series of pixel intensity changes measured at a single pixel ("+") shown in (a). The raw signal intensity is shown as dotted lines for the RBC (green) and plasma (red) images. Signal intensity changes were sufficient to determine both appearance and disappearance times after filtering the shot noises (straight line). Representative images for the appearance (c) and disappearance (d) times measured on a single-pixel basis shown in (a). Fast appearance and disappearance were observed in the arterial vessels (red), whereas the large veins (green to blue) had slow appearance and disappearance. Note that longitudinal traces along the vessel were seen for the large veins, indicating the parallel flow in these vessels.

compartments (Fig. 2a). From all five animals, we obtained a total of 423 vessel segments (i.e., 145 artery and 278 vein segments, Table 1), which can be considered as a sufficient number of samples for comparative statistical analysis between control and perturbation conditions. The mean pixel occupancy per image was 7.1%, 4.1%, and 0.7% for the arterial segments LA, MA, and SA, respectively, whereas it was 5.0%, 8.8%, and 21% for the venous segments SV, MV, and LV, respectively (Table 1). The mean number of the vessels analyzed for all 6 segments is also summarized in Table 1. In case of mis-prediction after automated segmentation, such as for an intersection of an artery and a vein, manual corrections were made with reference to the original time-lapse images (Fig. 2b).

The appearance time histogram showed two sharp peaks corresponding to the artery and vein signals (Fig. 2c). In contrast, the disappearance time histogram showed a broad, mixed distribution (Fig. 2d). Because the mixture of the artery and vein signals makes it difficult to differentiate the two, only appearance time results were used for later analysis.

Global perturbation

Comparison between control (Fig. 3a1) and SNP conditions (Fig. 3a2) showed an increase in the fluorescent agent passages after SNP induction, largely in the arterial side. The average increases in the arterial widths were 9 ± 7 and 5 ± 7 μm for the RBC and plasma passages, respectively, in this representative animal, where the arterial baseline widths were 24 ± 13 and 31 ± 13 μm for the RBC and plasma passages, respectively (Fig. 3b1). On the other hand, the venous vessel RBC and plasma widths were 54 ± 59 and 60 ± 60 μm, respectively, under control conditions, and 56 ± 60 and 58 ± 59 μm, respectively, under SNP conditions (Fig. 3b2). The statistically significant ($p<0.01/4$, paired *t*-test with Bonferroni correction) increase in the width changes due to SNP were detected for the arterial compartment, but not the venous side, in both RBC and plasma measurements. It should be noted that a relatively wide width was detected for the plasma compared to the RBC passages (Figs. S2a1 and S2a2).

A marked increase in the appearance time was also detected in all vein segments after SNP injection (Figs. 3a1 and a2). The average increase was 1.4 ± 0.5 and 1.5 ± 0.6 s for RBC and plasma, respectively, in the veins (Fig. 3c2), whereas it was 0.25 ± 0.22 and 0.28 ± 0.19 s in the arteries (Fig. 3c1). Tease differences between the control and SNP conditions were statistically significant ($p<0.01/4$) for both artery and vein components. Consequently, the difference in the mean appearance time between artery and vein compartments also increased: control vs. SNP appearance times were 1.0 vs. 2.2 s for

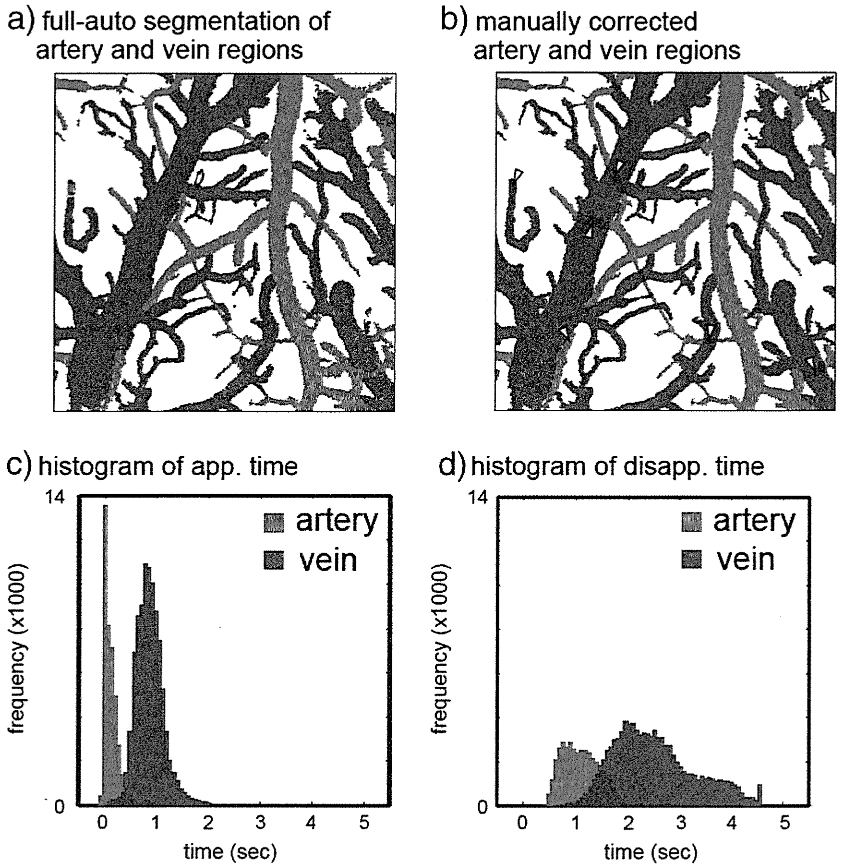

Fig. 2. Segmentation and histogram measurements. (a) Representative raw images after automatic segmentation. The artery (red) and vein (blue) areas were masked out by the region-growing technique by referencing appearance time results. (b) The masks were manually corrected for intersection and error regions (arrowheads) by referencing the original time-lapse image. Histograms of the appearance and disappearance times are shown in (c) and (d), respectively. The red and blue populations represent the pixels in the arterial and venous masked regions, respectively. Due to the large overlap of the artery and vein pixels in the disappearance time measurements, only the appearance time measurements were used for later analysis.

RBC and 0.8 vs. 2.1 s for plasma, indicating an extended traveling time through parenchymal microcirculation under SNP conditions. The similar trend was detected in the changes of appearance time for RBC and plasma in the both arteries (Supplemental Fig. S2b1) and veins (Supplemental Fig. S2b2).

Local perturbation

Width changes of the fluorescent signal passages were not evidently observed for the response to forepaw stimulation (Fig. 4a2) relative to the control condition (Fig. 4a1). Vessel-by-vessel comparisons showed that the widths under control vs. local perturbation conditions were 40 ± 17 vs. 37 ± 18 μm for RBC and 42 ± 17 vs. 42 ± 18 μm for plasma in arteries (Fig. 4b1), and 57 ± 60 vs. 59 ± 60 μm for RBC and 64 ± 59 and 63 ± 58 μm for plasma in veins (Fig. 4b2), respectively. On the other hand, the venous appearance time decreased (0.7 ± 0.2 s) equally for both RBC and plasma (Fig. 4c2), whereas the mean difference in the arterial appearance time between control and forepaw stimulation was 0.17 ± 0.09 s and 0.13 ± 0.07 s for RBC and plasma (Fig. 4c1), respectively. The similar trend was detected in the width changes (Supplemental Figs. S3a1 and a2) and appearance time (Supplemental Figs. S3b1 and b2) between RBC and plasma passages.

Width changes: global vs. local perturbation

Population data showed that global perturbation induced significant vasodilation in the arteries (15 ± 9 and 15 ± 12 μm) as well as the veins (10 ± 8 and 7 ± 10 μm) for both RBC and plasma, respectively. These changes were uniform among the vessel segments, leading to relatively higher change ratios in the small arteries due to the smaller widths at their baseline (Fig. 5a1). The SA compartment showed average increases of 89% and 79% in the RBC and plasma

Table 1
Segmented vessel properties (N = 5).

	LA	MA	SA	SV	MV	LV
Mean width (μm)	64 ± 6	35 ± 2	19 ± 3	32 ± 3	66 ± 1	188 ± 35
Total number of vessels	23	73	49	176	75	27
Mean number of vessels per image	5 ± 2	15 ± 8	10 ± 5	35 ± 9	15 ± 4	5 ± 2
Mean number of pixels per vessel	4540 ± 1957	713 ± 160	212 ± 75	359 ± 73	1644 ± 556	10,339 ± 3417
Mean occupancy per image (%)	7.1 ± 2.6	4.1 ± 3.0	0.7 ± 0.3	5.0 ± 2.1	8.8 ± 1.4	21 ± 8

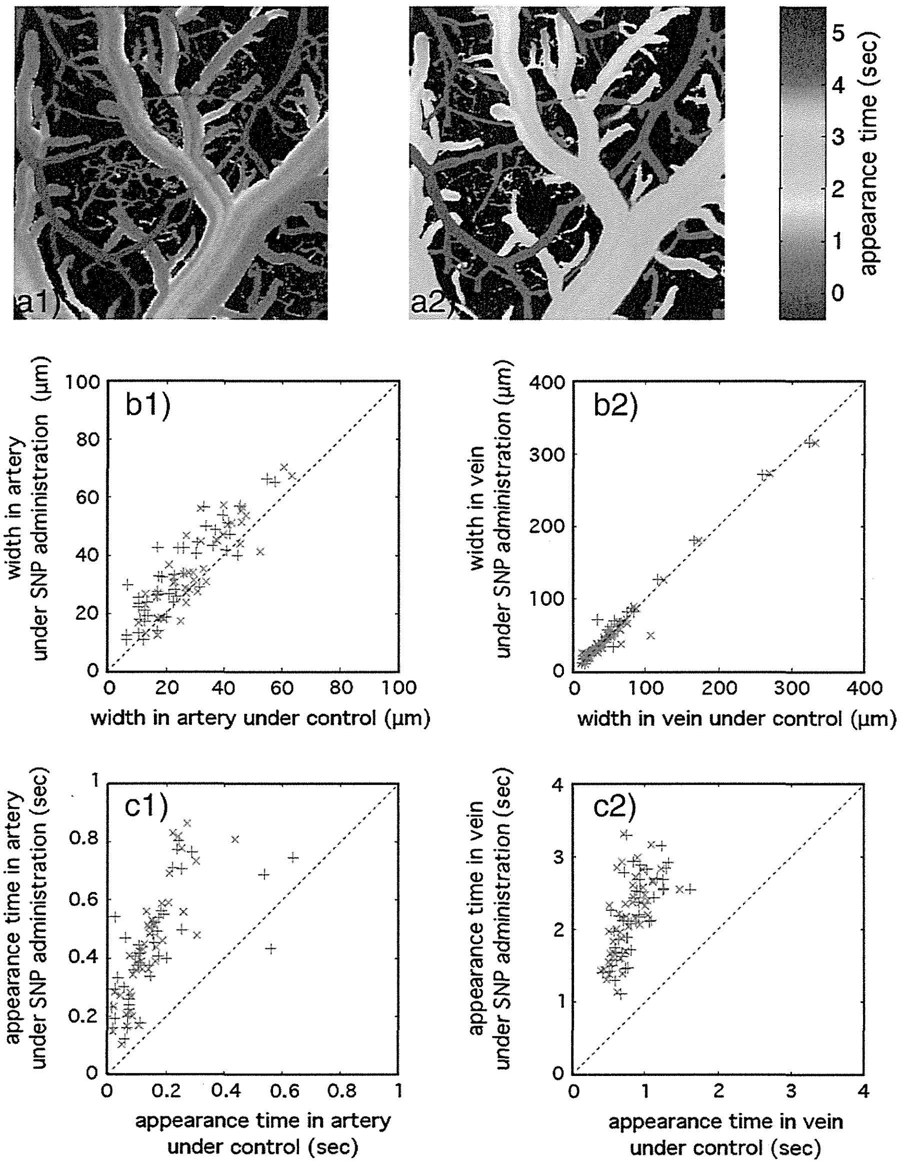

Fig. 3. Representative results for global perturbation measurements (N = 1). (a) Plasma appearance times are shown for control (a1) and SNP (a2) conditions. The color differences between the two images indicate the SNP-induced increase in the venous appearance time (orange/yellow to green/blue). Further, the SNP induced vasodilation in both the arterial (red) and venous segments (orange/green). (b) A comparison of the width changes induced by SNP for all arterial (b1) and venous (b2) segments. A consistent increase in the width was seen for both the RBC (green "+") and plasma (red "x") passages. (c) A comparison of the appearance time measurements. The SNP increased the appearance time slightly in the arteries (c1) and increased the appearance time greatly in the veins (c2).

widths, respectively: these were the largest changes among all 6 vessel segments. For local perturbation (Fig. 5b1), large arteries and veins showed no significant changes in width for either RBC (1.7 ± 4.7 and − 0.2 ± 5.8 µm) or plasma (1.9 ± 5.1 and 0.5 ± 5.6 µm), while the small arteries and veins showed significant dilation (2.3 ± 4.9 and 2.3 ± 4.2 µm for RBC and 4.1 ± 4.1 and 2.7 ± 6.0 µm for plasma, respectively). As a result, the SA had the highest increases in the vessel width induced by local perturbation; 13% and 18% increase for RBC and plasma, respectively.

Appearance time changes: global vs. local perturbation

Dependence on vessel size was not observed for changes in appearance time induced by either global (SNP injection) or local (forepaw stimulation) perturbations. SNP injection induced a relatively uniform increase in the venous appearance time (Fig. 5a2). A significant increase was observed in the MA, SA, SV, and MV compartments (0.2 to 1.0 s). In contrast, forepaw stimulation significantly shortened the venous appearance time (− 0.5 to − 0.4 s, Fig. 5b2). The SA and SV compartments consistently had the largest gap for both perturbations, indicating that the changes in the appearance time mostly originate from parenchymal microcirculation. To further investigate the contribution of parenchymal microcirculation to the changes induced by SNP, the time differences between the end point of the SA and the starting point of either the SV or MV compartments were measured. The results showed that the average differences in the RBC appearance time were 0.8 ± 0.4 and 0.9 ± 0.5 s in SA–SV and SA–MV, respectively, under control conditions, and increased to 1.4 ± 0.1 and 1.5 ± 0.2 s following global perturbation. Similarly, the differences in the plasma appearance time were 0.7 ± 0.4 and 0.8 ± 0.5 s for SA–SV and SA–MV, respectively, under control conditions, and increased to 1.2 ± 0.3 and 1.2 ± 0.2 s under global perturbation. These

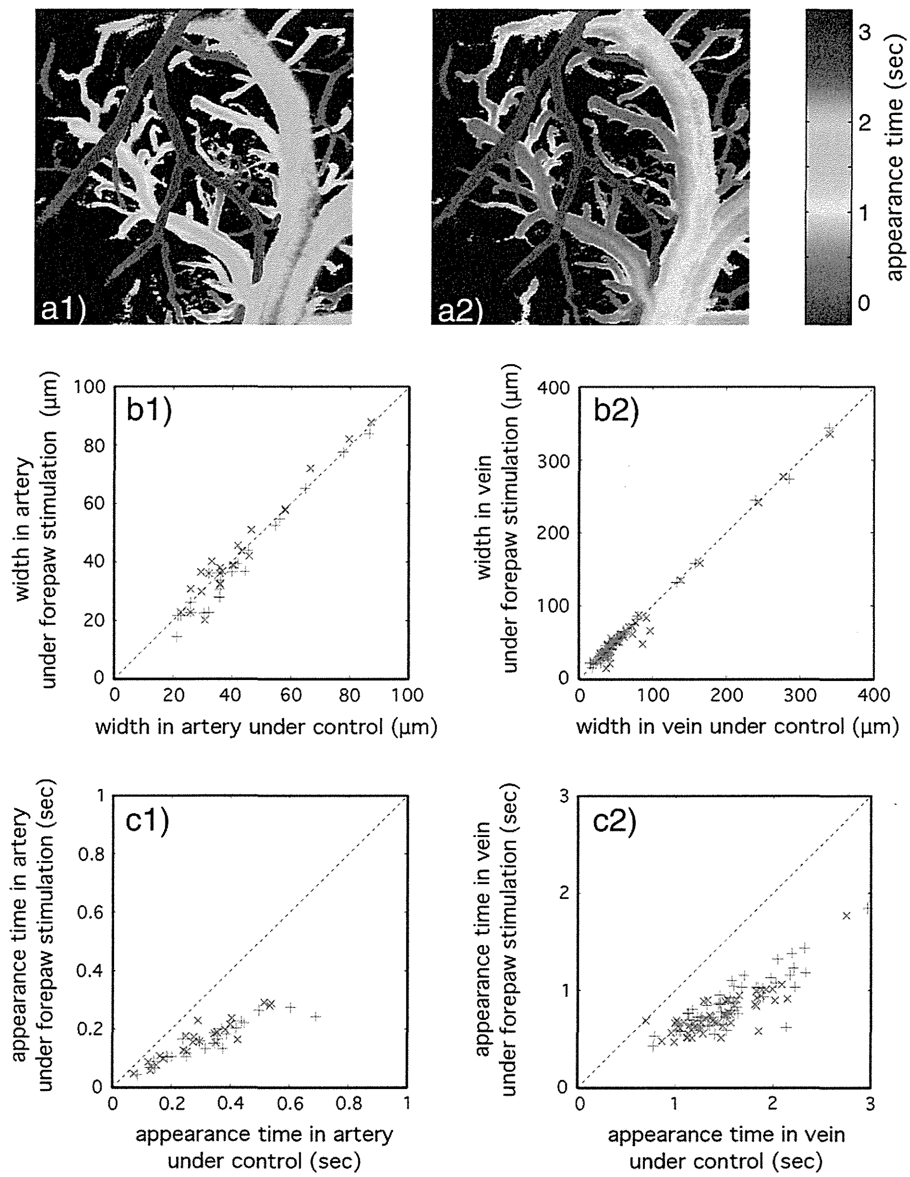

Fig. 4. Representative results for local perturbation measurements (N = 1). (a) Plasma appearance times are shown for control (a1) and forepaw stimulation (a2) conditions. The venous segments showed shortening of appearance time (green/blue to orange/yellow). Changes in vessel width were not evident. (b) Similar widths were maintained for forepaw stimulation in all artery (b1) and venous (b2) segments. The RBC and plasma results are represented as green "+" and red "x", respectively. (c) A comparison of the appearance time measurements. Forepaw stimulation shortened the appearance time slightly in the arteries (c1) and shortened the appearance time greatly in the veins (c2).

results show a large increase in the parenchymal traveling time: there were 0.56 and 0.56 s increases in the RBC appearance times for SA–SV and SA–MV, respectively, and 0.49 and 0.38 s increases in the respective plasma appearance times.

Discussion

To distinguish the vessel type and segments, the present study focused on the spatiotemporal continuity of the fluorescent signal changes measured using high-speed confocal microscopy on a per-pixel basis and across neighboring pixels (Fig. 1), which allowed automatic segmentation without applying spatial filtering (Fig. 2). Because the algorithm relies on the spatial continuity and separability of the fluorescent signal transits within and between the artery and vein compartments, the extension to three-dimensional segmentation can be possible if the signal source originating from the artery and vein components was identified across the different planes. By using a mixed tracer of the fluorescently-labeled RBC and plasma, the present method further allowed cross-image comparisons of the both vessel-by-vessel RBC and plasma passages (Figs. 3 and 4). The demonstrative results showed that the image-based analysis of the flow dynamics provides large numbers of data points for small to large vessels (i.e., about 30 arteries and 55 veins per image, Table 1) and reveals the spatial coherence of the vessel size and type dependent responses (Fig. 5).

Responses to global vs. local perturbation

We observed an identical extension of the RBC and plasma width following the SNP induction (Fig. 5a), which indicates a parallel width shift for RBC and plasma. To confirm this observation, a single-pixel-basis correlation analysis was further performed (Supplemental Fig. S4). The results showed no detectable differences of the RBC and plasma profile changes in the radial directions, i.e. no

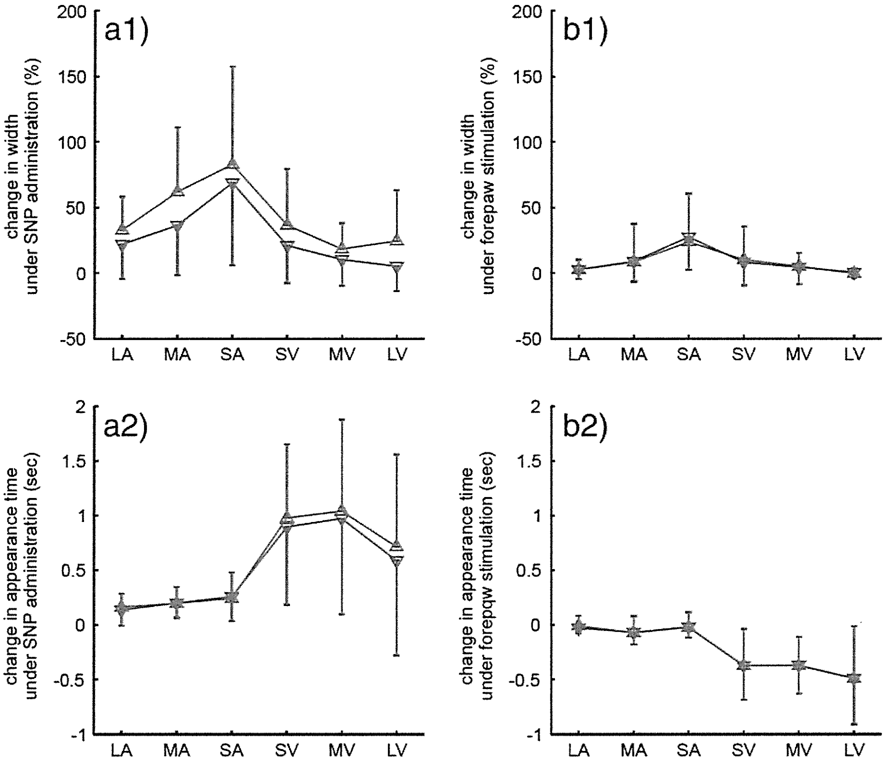

Fig. 5. Width and appearance time changes. The responses to global (a) and local (b) perturbation were compared across all 6 segments; LA: large arteries (>50 μm in a diameter), MA: medium arteries (>25, <50 μm), SA: small arteries (<25 μm), LV: large veins (>100 μm), MV: medium veins (>50, <100 μm), and SV: small veins (<50 μm). The results of the RBC (green) and plasma (red) measurements are indicated as upward-pointing and downward-pointing triangles, respectively. SNP induced vasodilation for all vessels (a1). The largest change was observed for the SA, which was consistent with the forepaw stimulation response (b1). In contrast, different responses to the SNP and forepaw stimulation were seen for the appearance time measurements (a2 and b2). The SNP increased venous appearance time (b2), whereas the forepaw stimulation decreased it. The difference could be related to changes in systemic blood pressure under two conditions. Nevertheless, both conditions provoked the largest gap between SA and SV, which indicate that the changes mostly originate from parenchymal microcirculation. Error bar: standard deviation.

changes in hematocrit level, between control and SNP conditions. The correlation image also showed a thin layer of the intermediate correlation pixels (0.4 to 0.6) near the interface between the vessel and tissue areas. Because the correlation is high (>0.8) in the vessel areas and low (<0.1) in the tissue areas, the lowered correlation indicates dissociation of the RBC and plasma signals (i.e., a plasma layer). The thickness of this layer was measured as 4 to 6 μm, which was slightly larger than the reported size of the plasma layer; 1 to 3 μm in the rat cremaster muscle arteries (Kim et al., 2007), about 3 μm in the rabbit omentum microvessels (Schmid-Schoenbein and Zweifach, 1975), and 4 μm in cat cerebral microvessels (Yamaguchi et al., 1992). The difference between the present and previous reports could be related to the low pixel resolution (3.6 μm/pixel) of our measurements. At the border areas of the vessels, signal to noise ratio tends to be low due to partial volume effects, which may also contribute to the overestimation.

The results of significant vasodilation seen in both arteries and veins under SNP conditions are in good agreement with previous reports (Auer, 1978). On the other hand, local perturbation induced vasodilation in the small arteries, which are also consistent with previous reports (Drew et al., 2011; Vanzetta et al., 2005). The differences in the responses to the two types of perturbation were further revealed in our measurements of the appearance time that showed both an extension and shortening depending on the perturbation. The change of venous appearance time indicates a change of flow speed or traveling distance through parenchymal microcirculation. Because both perturbations induced upstream arterial dilation, the shortening of the traveling distance (i.e., hypoperfusion) is not likely. Thus, the shortened venous appearance time induced by forepaw stimulation indicates an increase in the flow speed (Kleinfeld et al., 1998; Stefanovic et al., 2007), whereas the extended venous appearance time during SNP administration could be due to a decrease in flow speed and/or an increase in the traveling distance. The SNP-induced decrease in the flow speed was further confirmed with correlation analysis of time-intensity curves in two cross-sections (Supplement Fig. S5). Under control conditions, the mean venous speed was 0.89 ± 0.39 and 0.97 ± 0.42 mm/s for the RBC and plasma, respectively ($n = 10$ from one representative animal, Supplemental Fig. S6). Following SNP induction, the mean venous speed decreased to 0.46 ± 0.24 and 0.50 ± 0.29 mm/s for the RBC and plasma, respectively. It should be noted that a slightly faster speed was detected for the plasma in these vessels. This observation contradicts previous reports measured in the cerebral microcirculation (Lin et al., 1995; Rovainen et al., 2003; Schiszler et al., 2000). The contradiction may be due to differences in the vessel size and type investigated. Further improvements of the spatial and temporal resolution for the image acquisition will enable us to provide detailed flow velocity maps, including arterial vessels, in future studies.

Implication for flow regulatory mechanisms in the parenchyma microcirculation

Another important aspect of our observations is that each longitudinal trace appearing in the venous vessel represents a different travel path of the blood through the parenchymal microcirculation. For example, a fast appearance in the venous trace represents a fast path in the parenchymal microcirculation. Considering the three-dimensional structure of the parenchymal microcirculation (Bär, 1981), it can be expected that a fast path represents a passage through subsurface regions (i.e., a short path), and a slow path represents a passage deep in the parenchyma (i.e., a long path). If the surface arteries primarily respond to cortical activation, the uniform increase in the parenchymal blood flow was expected. However, recent fMRI studies have shown that the earliest vasodilatory response to somatosensory stimulation was evoked at middle cortical layers in the anesthetized rats (Hirano et al., 2011; Tian et al., 2010), suggesting that the parenchymal blood flow was not solely regulated by the cortical surface arteries. Future studies must need to focus on the regulatory mechanism of the parenchymal microcirculation.

Furthermore, the dissociation between the RBC and plasma traces indicates a separation of the RBC and the plasma passages through the parenchymal microcirculation, which may be caused by plasma skimming and/or thoroughfare channels for RBC (Hasegawa et al., 1967; Hudetz et al., 1996; Safaeian et al., 2011). Although no significant differences in the RBC and plasma transit were observed for the appearance times in the present study, the disappearance times showed detectable differences. The average differences in the plasma disappearance times were 1.1 ± 0.5 and 1.6 ± 0.5 s under control conditions for SA–SV and SA–MV, respectively. Both increased by 0.4 s under global perturbation conditions: plasma disappearance times were 1.5 ± 0.9 and 2.0 ± 1.2 s for SA–SV and SA–MV, respectively. On the other hand, average RBC disappearance times were 1.1 ± 0.6 and 1.4 ± 0.6 s for SA–SV and SA–MV, respectively, under control conditions, and 2.1 ± 0.1 and 2.4 ± 0.2 s under global perturbation conditions. As a result, a large increase was seen in the RBC (1.0 s) disappearance time compared with the plasma (0.4 s) disappearance time under global perturbation, which differed from the appearance time results (0.6 and 0.5 s increase in the RBC and plasma appearance times, respectively). In addition, the fact that appearance is sensitive to a fast path, whereas the disappearance is more sensitive to a slow path, indicates that the RBC circulation shifts to the deeper or longer pathways under SNP conditions. These findings clearly show the dissociation of the RBC and plasma passages in the parenchymal microcirculation. With variable perturbations to the model animals, such as neurodegenerative diseases and aging models, future studies will allow further understanding of the role and mechanism of pathway (channel) specific blood flow regulation in the parenchymal microcirculation.

Conclusion

The image-based analytical method for time-lapse images of RBC and plasma dynamics with automatic segmentation was presented. The method enables us to quantify the perturbation-induced changes of the RBC and plasma passages in the individual vessels of the cortical surface and parenchymal microcirculation. Both SNP and forepaw stimuli induced arterial dilation on the cortical surface, whereas the slower and faster transits through the parenchymal microcirculation was observed, depending on the perturbation. The findings support the hypothesis that cortical surface arterial tones and parenchymal blood flow can be individually coordinated.

Supplementary data related to this article can be found online at http://dx.doi.org/10.1016/j.mvr.2012.05.001.

Disclosure

The authors have no conflicts of interest to disclose, and the funding sources had no role on the conduct of the research and preparation of the article.

Contributors

H.K., K.M., and I.K designed the study, K.M. performed experiments, H.K. analyzed data, H.K., K.M., H.I., and I.K. discussed data interpretation, and H.K., K.M., and I.K. wrote the manuscript.

Acknowledgments

This work was partially supported by the Grant-in-Aid for Young Scientists (B) (22700441) (H.K.) and Special Coordination Funds for Promoting Science and Technology (K.M.).

References

Auer, L., 1978. The action of sodium nitroprusside on the pial vessels. Acta Neurochir. (Wien) 43, 297–306.

Autio, J., Kawaguchi, H., Saito, S., Aoki, I., Obata, T., Masamoto, K., Kanno, I., 2011. Spatial frequency-based analysis of mean red blood cell speed in single microvessels: investigation of microvascular perfusion in rat cerebral cortex. PLoS One 6, e24056.

Bär, T., 1981. Distribution of radially penetrating arteries and veins in the neocortex of rat. In: Cervós-Navarro, J., Fritschka, E. (Eds.), Cerebral Microcirculation and Metabolism. Raven Press, New York, pp. 1–8.

Borowsky, I.W., Collins, R.C., 1989. Metabolic anatomy of brain: a comparison of regional capillary density, glucose metabolism, and enzyme activities. J. Comp. Neurol. 288, 401–413.

Drew, P.J., Shih, A.Y., Kleinfeld, D., 2011. Fluctuating and sensory-induced vasodynamics in rodent cortex extend arteriole capacity. Proc. Natl. Acad. Sci. U. S. A. 108, 8473–8478.

Fukuda, M., Wang, P., Moon, C.H., Tanifuji, M., Kim, S.G., 2006. Spatial specificity of the enhanced dip inherently induced by prolonged oxygen consumption in cat visual cortex: implication for columnar resolution functional MRI. NeuroImage 30, 70–87.

Haberl, R.L., Heizer, M.L., Marmarou, A., Ellis, E.F., 1989a. Laser-Doppler assessment of brain microcirculation: effect of systemic alterations. Am. J. Physiol. 256, H1247–H1254.

Haberl, R.L., Heizer, M.L., Ellis, E.F., 1989b. Laser-Doppler assessment of brain microcirculation: effect of local alterations. Am. J. Physiol. 256, H1255–H1260.

Hasegawa, T., Ravens, J.R., Toole, J.F., 1967. Precapillary arteriovenous anastomoses. "Thoroughfare channels" in the brain. Arch. Neurol. 16, 217–224.

Hirano, Y., Stefanovic, B., Silva, A.C., 2011. Spatiotemporal evolution of the functional magnetic resonance imaging response to ultrashort stimuli. J. Neurosci. 31, 1440–1447.

Hudetz, A.G., Fehér, G., Kampine, J.P., 1996. Heterogeneous autoregulation of cerebrocortical capillary flow: evidence for functional thoroughfare channels? Microvasc. Res. 51, 131–136.

Kim, S., Kong, R.L., Popel, A.S., Intaglietta, M., Johnson, P.C., 2007. Temporal and spatial variations of cell-free layer width in arterioles. Am. J. Physiol. Heart Circ. Physiol. 293, H1526–H1535.

Kim, T., Masamoto, K., Fukuda, M., Vazquez, A., Kim, S.G., 2010. Frequency-dependent neural activity, CBF, and BOLD fMRI to somatosensory stimuli in isoflurane-anesthetized rats. NeuroImage 52, 224–233.

Kleinfeld, D., Mitra, P.P., Helmchen, F., Denk, W., 1998. Fluctuations and stimulus-induced changes in blood flow observed in individual capillaries in layers 2 through 4 of rat neocortex. Proc. Natl. Acad. Sci. U. S. A. 95, 15741–15746.

Larson, D.R., Zipfel, W.R., Williams, R.M., Clark, S.W., Bruchez, M.P., Wise, F.W., Webb, W.W., 2003. Water-soluble quantum dots for multiphoton fluorescence imaging in vivo. Science 300, 1434–1436.

Lin, S.Z., Chiou, T.L., Chiang, Y.H., Song, W.S., 1995. Hemodilution accelerates the passage of plasma (not red cells) through cerebral microvessels in rats. Stroke 26, 2166–2171.

Masamoto, K., Kim, T., Fukuda, M., Wang, P., Kim, S.G., 2007. Relationship between neural, vascular, and BOLD signals in isoflurane-anesthetized rat somatosensory cortex. Cereb. Cortex 17, 942–950.

Masamoto, K., Vazquez, A., Wang, P., Kim, S.G., 2008. Trial-by-trial relationship between neural activity, oxygen consumption, and blood flow responses. NeuroImage 40, 442–450.

Mchedlishvili, G., 1986. Chapter 4. Regulation providing an adequate blood supply to cerebral tissue. In: Bevan, J.A. (Ed.), Arterial Behavior and Blood Circulation in the Brain. Plenum Press, New York, pp. 96–175.

Nishimura, N., Schaffer, C.B., Friedman, B., Lyden, P.D., Kleinfeld, D., 2007. Penetrating arterioles are a bottleneck in the perfusion of neocortex. Proc. Natl. Acad. Sci. U. S. A. 104, 365–370.

Park, S.H., Masamoto, K., Hendrich, K., Kanno, I., Kim, S.G., 2008. Imaging brain vasculature with BOLD microscopy: MR detection limits determined by in vivo two-photon microscopy. Magn. Reson. Med. 59, 855–865.

Reniers, D., van Wijk, J., Telea, A., 2008. Computing multiscale curve and surface skeletons of genus 0 shapes using a global importance measure. IEEE Trans. Vis. Comput. Graph. 14, 355–368.

Rosenblum, W.I., Kontos, H.A., 1974. The importance and relevance of studies of the pial microcirculation. Stroke 5, 425–428.

Rovainen, C.M., Woolsey, T.A., Blocher, N.C., Wang, D.B., Robinson, O.F., 2003. Blood flow in single surface arterioles and venules on the mouse somatosensory cortex measured with videomicroscopy, fluorescent dextrans, nonoccluding fluorescent